1991

A parametric study of the factors affecting strain levels in electronic packages

Pei-Haw Tsao
Lehigh University

A PARAMETRIC STUDY

OF

THE FACTORS AFFECTING STRAIN LEVELS

IN

ELECTRONIC PACKAGES

by

Pei-Haw Tsao

A Thesis

Presented to the Graduate Committee

of Lehigh University

in Candidacy for the Degree of

Master of Science

in

Mechanical Engineering

Lehigh University

1990

Certificate of Approval

This thesis is accepted and approved in partial fulfillment of the requirements for the degree of Master of Science in Mechanical Engineering

12/17/90

Date

Prof. Arkady S. Voloshin

Adviser

Prof. Robert P. Wei

Chairman of Department

Acknowledgements

I am grateful to Prof. Arkady S. Voloshin for his continuous guidance, encouragement and valuable advice. This research would not be done without his help. Appreciations are due Dr. A.F. Bastawors for his assistance, *CYPRESS* Semiconductor Inc. for their support in specimen preparation. The SRC support through the grant to Lehigh University in greatly appreciated.

Finally, a special thank is due my wife, Mei-Li, for her generous support and tireless typing.

Table of Contents

List of Tables

List of Figures

Nomenclature

α :Coefficient of thermal expansion

β :Intersection angle

γ_{xy} :Shear strain in Cartesian coordinates

ε_x :Normal strain in x-direction in Cartesian coordinates

$\varepsilon_{x,m}$:Net mechanical strain in x-direction

ε_y :Normal strain in y-direction in Cartesian coordinates

$\varepsilon_{y,m}$:Net mechanical strain in y-direction

ε_1 :Principal strain in the first direction

ε_2 :Principal strain in the second direction

λ :Wavelength of light

$\phi(x)$:Continuous fringe order

f :Grating frequency

$I(x)$:Light intensity at point x

I_0 :Background light intensity

I_1 :Amplitude of the first cyclic component of light intensity

I :A function of $I(x)$,I_0 ,and I_1

N :Fringe order

N_x :Fringe order in the U-field

N_y :Fringe order in the V-field

T :Temperature

U :Displacement component in Cartesian coordinates

V :Displacement component in Cartesian coordinates

Abstract

An experimental method is presented for the detection of thermally induced strains in electronic packages. The method uses Fractional Fringe Moiré Interferometry enhanced by Digital Image Processing. Unlike previous experimental techniques, which are unable to treat the small scales of the deformations in electronic packages, this technique is a sensitive, full field displacement measurement tool possessing high sensitivity and excellent spatial resolution. In contrast to analytical and numerical methods the technique monitors the actual displacements, requires no simplifying assumptions and operates on complex geometries. Furthermore, relatively small regions, such as chip corners which are thought to be high strain concentration zones, are easily examined.

The specimens investigated in this effort were prepared from *CYPRESS* devices and consisted of chips of different sizes, both with and without coatings. The chips were uniformly heated to *90° C* using special equipment and their thermal strains were monitored at selected planes. The resulting moiré patterns were analyzed by means of a fast and accurate data processing software. Larger chips were found to possess lower strains and the coating proved effective in reducing thermal strains by up to *35%*.

Chapter 1 : Introduction

Analytical, numerical, and experimental methods are available for the study of thermal strains in electronic packages. Analytical methods have progressed greatly and have expanded their range of applicability. As the complexity of the problem increases (through more sophisticated geometry or boundary conditions), however, part or all of the solution procedure of the analytical problem must be handled by numerical means.

When solving these analytical or numerical problems, either the solution is made possible or the solution procedure is simplified by the introduction of a set of assumptions. The question therefore is whether the problem solved is still reasonably representative of the original one. Experimental validation is then needed to verify the problem's formulation or solution procedure. Thus, experimental methods appear to be the ultimate validation procedure for analytical and numerical methods. However, the reliability of experimental methods lie in turn in the quality of the techniques employed. The objective of the experimentalist, therefore, is to minimize errors and acquire reliable, accurate data.

In this respect, and in connection with thermally induced strains in

electronic packages, the present work aims at applying an accurate and sensitive experimental methodology for displacement measurements. Chip size and coating will be the parameters under study. The following section provides a brief review of interferometric moiré method.

1.1 Moiré Interferometry

Guild [1] shows that all moiré phenomena may be treated as cases of optical interference, although moiré interferometry is actually a combination of optical and geometrical moiré. Thus, moiré techniques are all related. Moiré interferometry was first introduced by Post[2] in 1980 as a high resolution displacement measuring technique. Procedures for producing high frequency specimen gratings were also proposed. Moiré interferometry has been shown to be a very sensitive method for whole-field, in-plane displacement measurement. The technique possesses excellent attributes of contrast, range, spatial resolution, and sensitivity where many other techniques only excel in one of these areas. More recently, several improvements have been made including: setups for U and V measurements [3] and [4], optical separation of U and V fields [5], simpler optical systems [6], measurements of out-of-plane displacements, and better methodologies

for specimen grating production [7]. The introduction of this technique has led to an order of magnitude advancement in the capability of displacement measurements. Due to this high accuracy, Moiré interferometry is quite suitable for direct strain determination by differentiation and as a result is widely used.

In Figure 1.1 , a schematic describing moiré interferometry is given. A and B represent two coherent light rays which illuminate the specimen grating at angles +β and -β. At the intersection of the two light rays, an interference pattern is formed consisting of alternating constructive and destructive interference. This pattern is known as the virtual grating. At the specimen surface, the virtual grating is cut to produce a series of closely spaced fringes. These parallel fringes are simply alternating light and dark bands. The array of fringes and the interference pattern is termed the virtual reference grating. The equation for two beam interference gives the fringe frequency, f

$$f=(2/\lambda)\sin\beta \tag{1.1}$$

There are two types of specimen grating used in moiré method. One is amplitude gratings which consist of opaque bars and transparent spaces, the other is diffraction type (phase type) gratings, as shown in Figure 1.2.

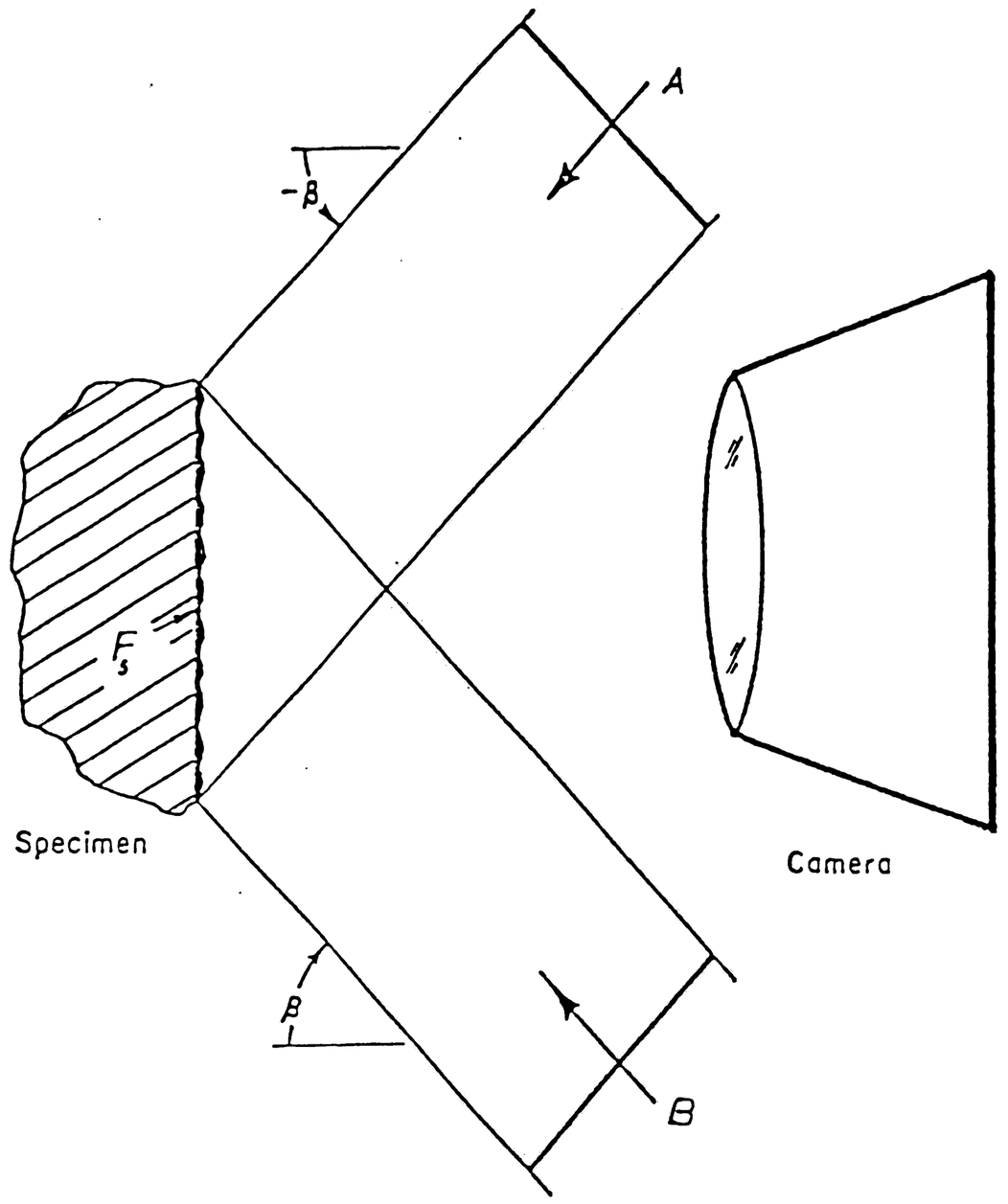

Figure 1.1 Schematic diagram of moiré interferometry.

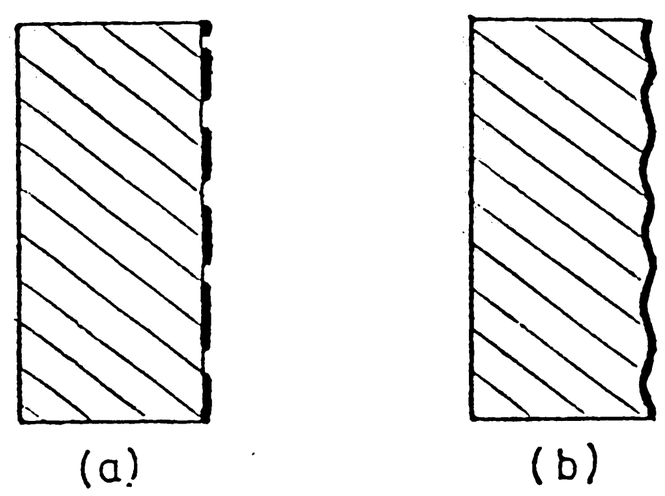

Figure 1.2 Diffraction gratings, (a) amplitude type and (b) phase type.

Because of low frequency, amplitude grating is mainly used in geometry moiré. Interferometric moiré enable to monitor the small order of displacement since a high frequency diffraction grating is created on the specimen surface. The grating is securely attached to the specimen and deforms with the specimen as loading is applied.

The specimen grating interacts with the virtual reference grating to form a moiré pattern. In order to have first order diffraction, the initial frequency of the specimen, f_s , is equal to one half of the reference grating frequency which corresponds to a magnification factor of 2,($f = 2f_s$). As illustrated in Figure 1.1, all lines of the virtual reference grating which interact with the specimen grating and produce the *U*-displacement field are perpendicular to the *x-axis*. In practice, another pair of coherent incident beams can be used to form a reference grating perpendicular to the *y-axis* to interact with the corresponding array of lines of the crossed-line specimen grating and produce the *V*-displacement field.

Figure 1.3 shown, a representative pattern of moiré interferometry. This pattern characterizes the in-plane displacements of every point on the specimen surface as contour maps of equal-displacement fringes. Quantitatively, the following equation determines each point of the fringe

pattern

$$U = N_x / f$$
$$V = N_y / f \qquad (1.2)$$

where U and V are the components of displacement in the x and y directions, respectively; N_x and N_y are the fringe orders when lines of the reference grating are perpendicular to the x and y directions, respectively; and f is the frequency of the reference grating. The reference grating frequency f was $2400\ lines/mm$, which corresponds to a sensitivity $(1/f)$ of $0.417\mu m$ per fringe order. N_x and N_y are determined at the fringe centers either manually or with the aid of digitizing tablets. The data values are defined by the dark or bright fringe pattern centers. In addition to the high sensitivity aspect of the fringe patterns, the patterns are also characterized by high fringe contrast and extensive range which make this technique so powerful.

To allocate fringe orders, it is necessary to define a point of zero displacement as the reference point and assign $N = 0$ to the fringe passing through that point. Then, the adjacent fringes are numbered relative to that fringe. The reference point may be any point whose displacement is known. This could be a location on the boundary, a location where a load is applied, or a location on a symmetry axis of the specimen. Regarding the strain

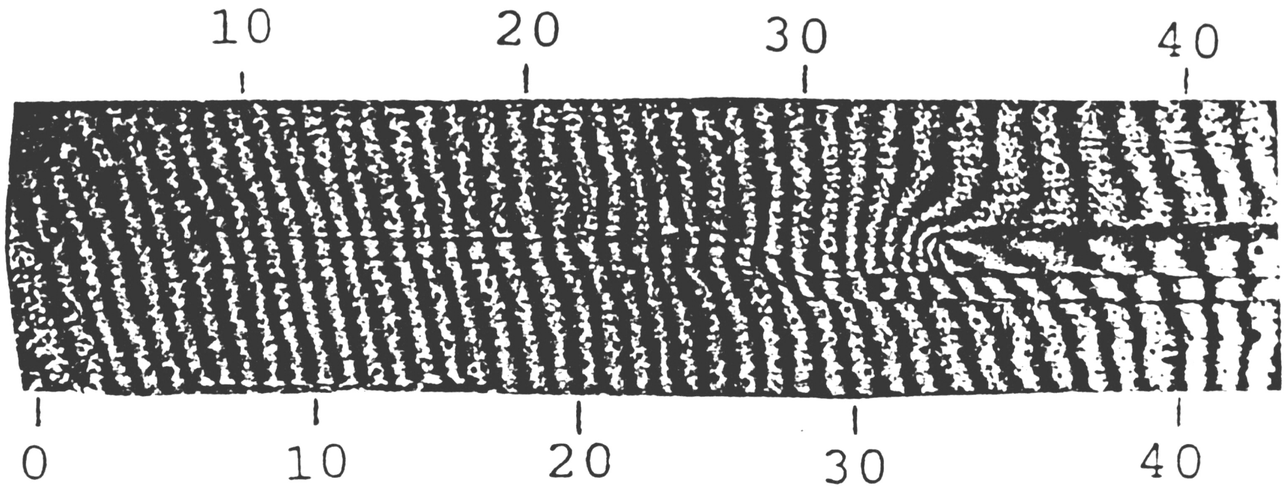

U

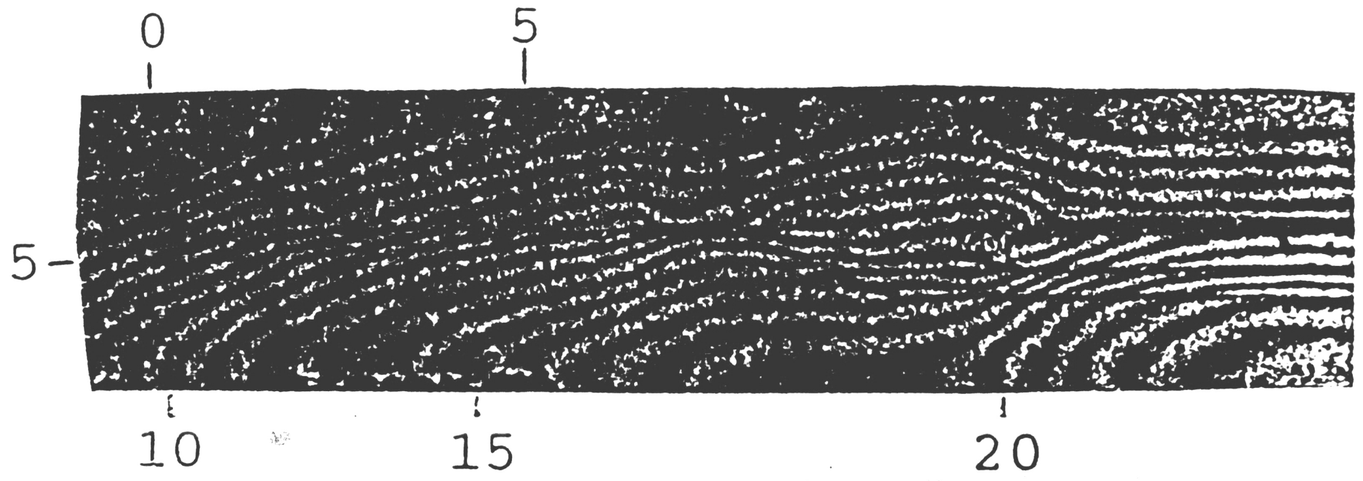

V

Figure 1.3 *U* and *V* fringe patterns for the cross-section of a thermally loaded electronic package.

analysis, only the relative displacements rather than the displacements themselves are of concern. Therefore, the actual location of a reference point is immaterial. Any arbitrary and convenient point crossed by a fringe can be considered a reference of zero order.The remaining fringes may then be calculated with respect to that reference fringe. Then, the displacement map according to this information can be produced. Once the displacement map has been constructed, strains may be determined from the strain-displacement relations as follows, assuming small strains

$$\varepsilon_x = \frac{\partial U}{\partial x} ,$$

$$\varepsilon_y = \frac{\partial V}{\partial y} , \qquad (1.3)$$

$$\gamma_{xy} = \frac{\partial U}{\partial y} + \frac{\partial V}{\partial x}$$

The derivatives in the right-hand side of equation (1.3) may be determined by measuring displacements of the specimen and approximated as:

$$\varepsilon_x = \frac{\Delta U}{\Delta x} ,$$

$$\varepsilon_y = \frac{\Delta U}{\Delta y} , \qquad (1.4)$$

$$\gamma_{xy} = \frac{\Delta U}{\Delta y} + \frac{\Delta V}{\Delta x}$$

In order to provide faithful representations of the derivative of the equation (1.4), Δx and Δy must be kept sufficiently small.

1.2 Specimen Gratings

Based on simple replication, illustrated schematically in Figure 1.4, the specimen grating is produced from a photographic mold. A pool of liquid adhesive is discharged on the surface of the specimen and then compressed into a thin film by pressing the specimen against the mold. After curing, the photographic mold is pried off very carefully with a small prying force and a reflective diffraction grating is bonded to the surface of the specimen. In general, the weakest interface of the sample will occur between the gelatin of the photographic plate and the evaporated aluminum or gold, which accounts for the transfer of the reflective film to the specimen. Based on the above procedure, a thin and reflective phase frequency type diffraction grating on the surface of specimen is formed. However, due to the replication scheme, the mold is lost. In order to preserve the mold for future applications, one must employ a different means to construct the specimen. Adding an intermediate replication step proves to be a more functional procedure that preserves the master mold for subsequent applications. Using this three-step process, a submaster is produced by replicating the phase

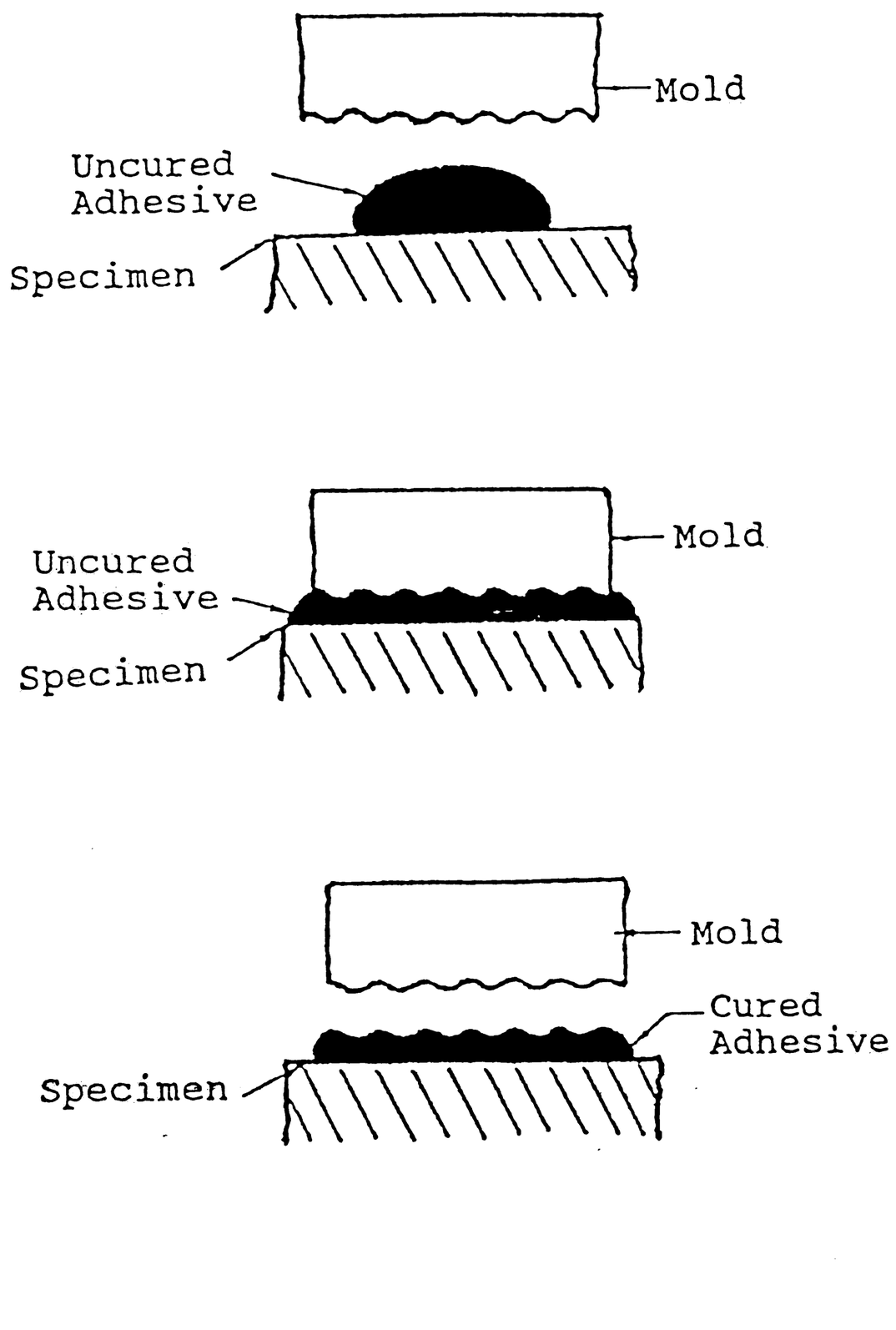

Figure 1.4 Steps for the preparation of specimen grating by a replication technique.

grating surface in silicon rubber, much in the same way as in Figure 1.4 ; the submaster is then used to replicate the phase grating in an adhesive on the specimen surface [8]. Silicon rubber of the liquid type has a distinct virtue for the intermediate step in that it is a nonadhesive replicating material. This permits easy separation from the master and also from the final specimen grating; it bonds well, however, to specially primed surfaces.

1.3 Moiré Interferometers

The optical system used to produce interferometric moiré fringes is called a moiré interferometer. Any method that brings coherent beams which are equivalent to *A* and *B* in Figure 1.1 into the specimen grating would suffice. According to Post[9], abundant optical designs can be contrived to form the virtual reference grating. A simple interferometer which is often referred to as a two-beam interferometer yields one displacement field. Here the specimen is illuminated by two beams to reproduce the arrangement of Figure 1.1. A better interferometer capable of giving two orthogonal displacement components is the so called four-beam interferometer, which is basically two sets of two-beam interferometers perpendicular to each other. Optical separation of the resulting moiré fields is necessary in this case to

arrive at the individual U and V fields. Examples of both types of interferometers are presented in following.

1.3.1 Two-Beam Interferometer

In Figure 1.5 , a specific arrangement is illustrated, where a thin collimated beam coming from the laser source is aimed into a small decollimating lens L, converged by the lens, and then passed through a spatial filter SF. The spatial filter, simply a pin-hole located at the focal point of the lens L, is adopted to eliminate any extraneous rays occurring within the laser beam. The divergent cone-like laser beam coming through the spatial filter is aimed at a parabolic mirror whose focal point is located at the pin-hole. This arrangement makes the light reflected from the mirror a clean wide collimated light beam. Then the resulting laser beam is projected at a proper angle β onto the specimen; half the incident beam impinges directly on the specimen surface, while the other half is reflected from a plane mirror and impinges on the surface from a symmetrical direction, $-\beta$. Light emerging normal to the specimen surface (responsible for fringe formation) is collected by the camera objective lens LC. This lens focuses the moiré fringe pattern as well as the surface of the specimen on the

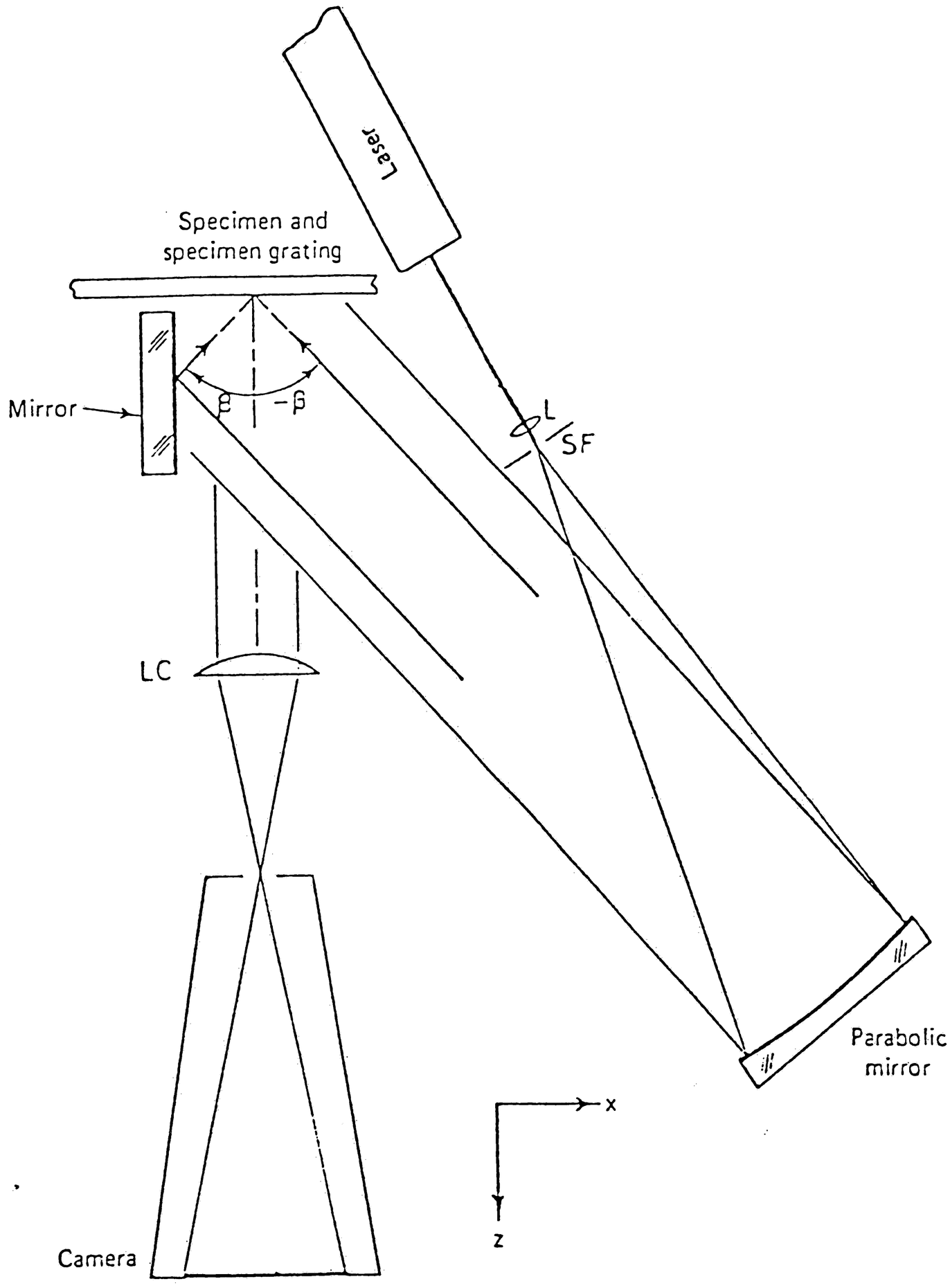

Figure 1.5 Optical arrangement for two-beam interferometer.

film plane or the camera sensor.

The above setup shown is sensitive to one displacement component only. If the other displacement component is desired then the same apparatus may still be used, but the specimen has to be rotated precisely *90°*. However, this is not practical in many cases, especially when relatively large and complex loading fixtures are used. A simple solution to this problem is the use of a four-beam interferometer which is described in the following section.

1.3.2 Four-Beam Interferometer

In order to measure both U and V displacement components directly without rotating any components, a four-beam interferometer may be employed. In this arrangement, the specimen is illuminated from four specific directions, where two of them produce one displacement field and the remaining two produce the other displacement field. A simple example of such an arrangement, is shown in Figure 1.6 [10], where two adjustable mirrors, A and B, are added into the basic system of Figure 1.5. The collimated beam coming from the parabolic mirror should be wide enough to

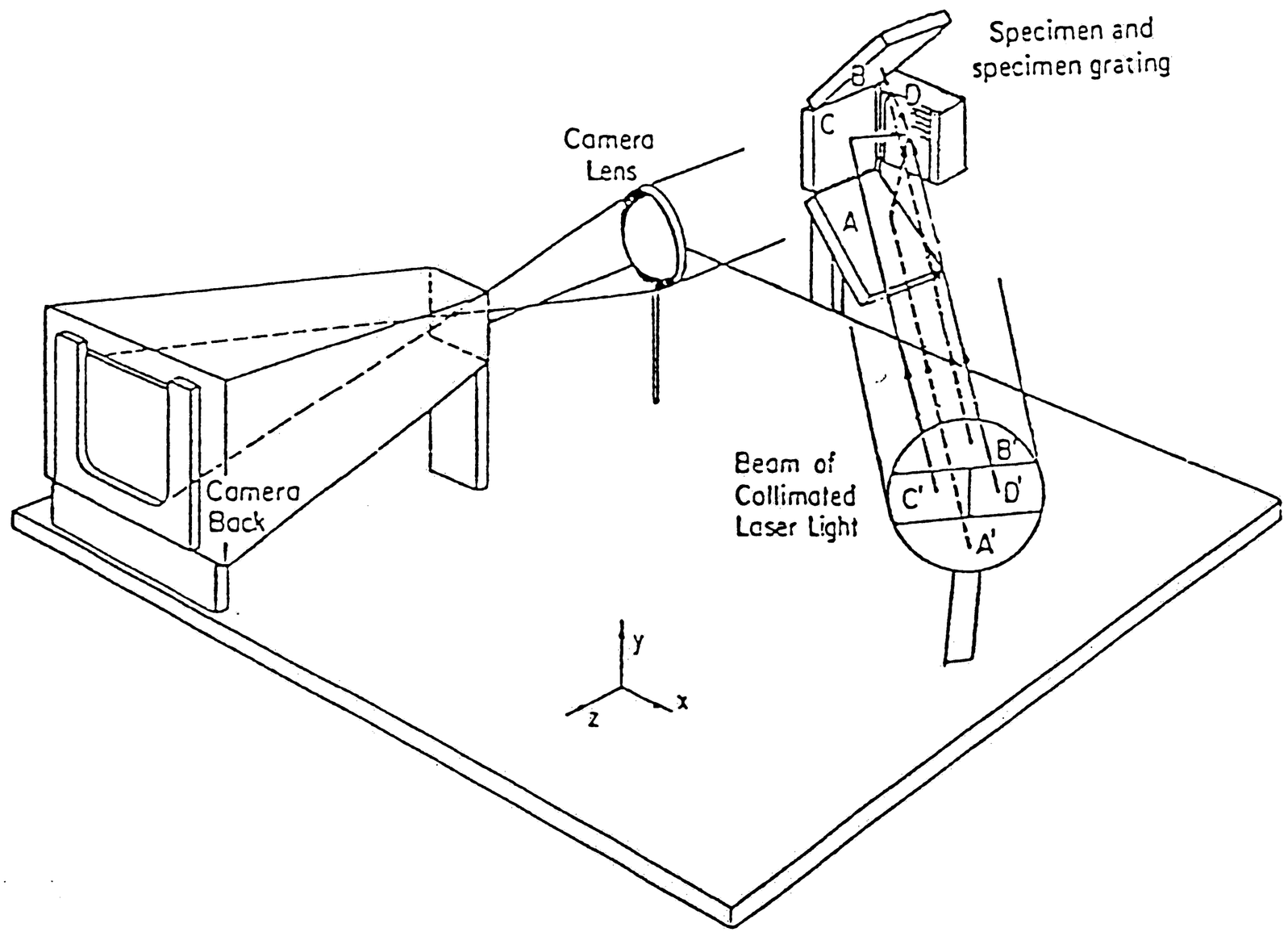

Figure 1.6 Optical arrangement for four-beam interferometer.

illuminate all three mirrors and the specimen simultaneously. According to the arrangement shown in Figure 1.6, if sections *A'* and *B'* of the incoming beam are blocked, the setup becomes identical to that of the two-beam interferometer discussed earlier, such that the fringe pattern collected at the film plane only reveals the *U* displacement pattern. Alternately, if one blocks sections *C'* and *D'* of the incoming beam and allows light from sections *A'* and *B'* to impinge on mirrors *A* and *B*, respectively, then the other displacement field will be displayed. In this arrangement, the laser beam is reflected from mirror *A* in an upward direction to lie on a plane parallel to the *yz-plane* and strike the specimen at an angle $+\beta$ relative to the *z-axis*. Simultaneously, light is reflected from mirror *B* downwards and strikes the specimen at an angle $-\beta$, in the same plane. Therefore, these two beams, from mirrors *A* and *B*, combine to construct a virtual reference grating with its walls of interference perpendicular to the *y-axis*. This reference grating interacts with the corresponding system of lines on the specimen grating to produce the *V* displacement field.

Obviously, this four-beam interferometer requires an additional mechanism to block the appropriate sections of the collimated beams. This could be as simple as inserting a piece of cardboard manually in the specific location, or an advanced mechanical shutter. However, a better way of

pursuing the same objective is to optically separate the two superposed fringe patterns as they emerge from the specimen and before they enter the camera [6]. Therefore, no mechanical obstruction of the beams is required. Instead, a polarizing beam splitter placed in the path of the rays emerging from the specimen, separates the two fields and directs them into two different directions where they can be recorded separately. This arrangement makes an intelligent use of the fact that the two fringe patterns are polarized in two orthogonal directions and can not pass through the same polarizer. This approach enables real-time simultaneous U and V measurements and is receiving wide acceptance.

1.4 Fractional Fringe Analysis

All moiré phenomena are cases of optical interference [1]. Regardless of whether they are produced by geometric moiré or interferometric moiré, Moiré fringes are formed by interference of light wavefronts; very much in the same way as for the two-beam interference. In addition, the analysis of the most general case of the two beam interference can be reduced to the following simple relation

$$I(x) = I_0 + I_1 \cos 2\pi f U(x) + \ldots\ldots\ldots + I_n \cos 2n\pi f U(x) \qquad (1.5)$$

where f is the reference grating frequency, $U(x)$ is the displacement at point x in a direction perpendicular to the grating lines, I_0 is a background intensity, $I_1, I_2, I_3, \ldots\ldots, I_n$ are harmonic components corresponding to the different diffraction orders contributing to the moiré pattern, and n is the maximum number of contributing diffraction orders.

A very important characteristic of moiré interferometry is that the fringe pattern is only due to interference of one diffraction order. The other diffraction orders do not contribute to the pattern. This further simplifies equation (1.5) to include only one diffraction pattern term. Therefore, the optical law of moiré interferometry becomes

$$I(x) = I_0 + I_1 \cos 2\pi f U(x) \qquad (1.6)$$

The definition of all parameters in the equation (1.6) is the same as that of equation (1.5). This provides a unique tool to illustrate the displacements as continuous functions of the light intensity distribution, and

thus creates a potential of extracting displacement data from moiré patterns if sufficient tools of measuring light intensities are available. However, in order to utilize equation (1.6), the quantities $I(x)$, I_0 and I_1 must be determined.

The optical law for moiré interferometry may be expressed in terms of the continuous fringe order $\phi(x)$ as follows

$$I(x) = I_0 + I_1 \cos 2\pi\phi(x) \tag{1.7}$$

rather than the displacement. It can be seen that each time $\phi(x) = n$, where n is an integer, the intensity will be a maximum (i.e. the center of a bright fringe). When $\phi(x) = 1/2\ (2n+1)$, the intensity will be a minimum (i.e the center of a dark fringe). A graphic illustration in Figure 1.7 exhibits the above relation. The bright fringes are the loci of points where the displacements, in the x-direction, of the specimen grating with respect to the reference grating are equal to an integer number multiplied by the pitch of the master grating. The dark fringes have similar interpretation, but in terms of the half pitches. When $\phi(x)$ is a multiple of one half, the displacement information is basically equivalent to that obtained by simply counting fringes. However, no such displacement information is available about other points in the field. For example, for a point a, in Figure 1.7,

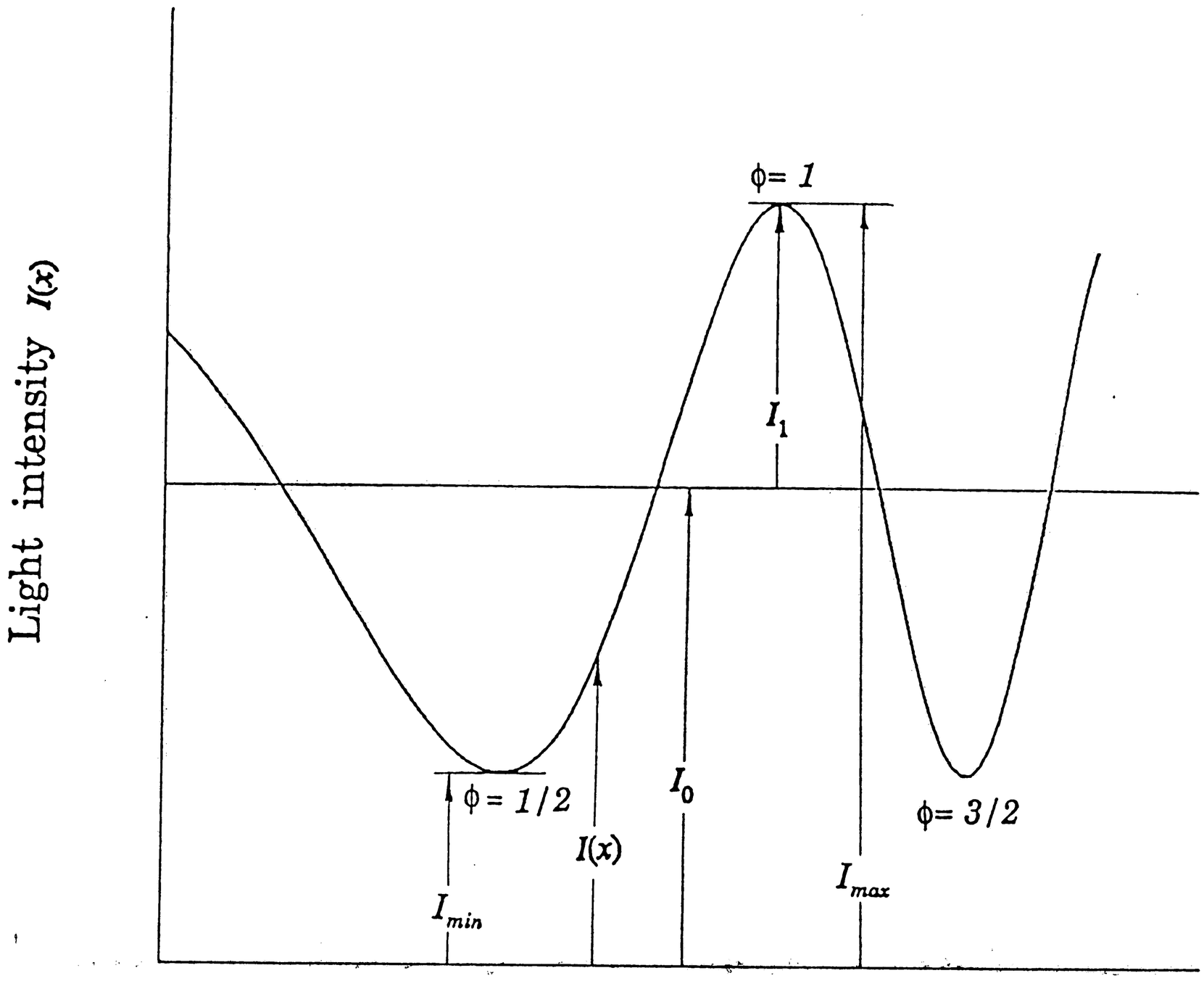

Figure 1.7 Light intensity distribution in moiré interferometry as represented by equation (1.7).

between the bright fringe at $\phi = 1$ and the dark fringe at $\phi = 3/2$, equation (1.7) must be applied to determine its displacement. Knowledge of the light intensity, $I(a)$, at that point together with the amplitudes I_0 and I_1 renders $\phi(a)$. The value of $\phi(a)$ will be a fraction between 0 and 1/2 and will yield the displacement at point a when multiplied by the pitch of the reference grating. The same argument is true for any intermediate point between any two fringes. This technique is known as Fractional Fringe Analysis [11]. Therefore, the fringe orders need not be multiples of 1/2; they may be any fractional number.

Equation (1.6) may be rewritten to directly yield the displacements as follows:

$$U(x) = (1/2\pi f) \cos^{-1} [(I(x) - I_0)/I_1] \qquad (1.8)$$

For simplicity the above equation may be applied over each half fringe separately, thus determining the displacements relative to the starting point. The actual cumulative displacements are found by adding the displacement of the starting points to all values determined.Mathematically, this is expressed as follows

$$U(x) = U_0 + (1/2\pi f) \cos^{-1} [(I(x) - I_0)/ I_1] \qquad (1.9)$$

where U_0 is the displacement at the starting point, and x is zero at that point. U_0 is the reference grating pitch multiplied by either an integer or an odd multiple of $1/2$, depending upon whether the starting point is a center of a bright or a dark fringe, respectively.

The amplitudes I_0 and I_1 are easily determined from light intensity distributions, such as that in Figure 1.7. I_0 is equal to $1/2(I_{max} + I_{min})$, and I_1 is $1/2(I_{max} - I_{min})$. Finally, the task of determining the displacement field has become that of determination of the light intensity field.

Chapter 2 : Facility And Experiment

Although moiré interferometry has been in use at Lehigh for only four years, a fully equipped Fractional Fringe Photomechanics laboratory has been established throughout the different phases of the research program. A four-beam moiré interferometer, high quality video and photography equipment, PC-based image processor and an anti-vibration optical table are examples of the facilities in the laboratory. In this chapter some components of the facility are introduced. Also the experiment is presented briefly.

2.1 Facility

2.1.1 The Interferometer

In order to measure the displacements for horizontal and vertical directions, the optical arrangement of the interferometer used, a four beam interferometer, is the same as that shown in Figure 1.6. The laser source used is a Spectra-Physics Helium-Neon laser, model *SP127-25*. It creates

25mW a *632.8 nm* wavelength laser beam whose diameter is *1.25 mm* . Also the laser ray is polarized. The decollimating lens, *L* (shown in Figure 1.5), which is a small double-convex lens of *6mm* diameter, has a *1.25 mm* focal length. It focuses the laser beam at the spatial filter, *SF* , which is a *50 μm* diameter pinhole. The filter is mounted on an *X-Y-Z* positioning stage which allows alignment of the filter at the focal position of the decollimating lens. Then, a parabolic mirror *108 mm* in diameter, is used to create a parallel laser beam of large diameter. The mirror is mounted on an adjustable stage such that the distance between the filter and the mirror is *867 mm*, the focal length of the parabolic mirror. The remaining mirrors used to direct the laser at particular angles are all first surface coated mirrors. All optical components used in the setup are of high optical quality *(λ/20)*.

In order to achieve critical alignment of the interferometer, most elements of the system should permit precise angular adjustments in certain directions. Thus, the flat mirrors (*A,B and C* in Figure 1.6) should rotate about two perpendicular axes in their own plane. In this respect, high precision mirror mounts made by Edmund Scientific Co. are used. The loading frame should also be mounted on a stage allowing fine rotation of the whole frame about an axis normal to the specimen surface, in order to have the specimen rotate with respect to the flat mirrors. Furthermore, control of

the incidence angle β on the whole assembly (all mirrors and specimen) is required. Therefore the mirror mounts and the loading frame are mounted in turn on a third stage allowing precise rotation of the assembly. Performing the adjustments mentioned ensures the correct alignment of the interferometer; special care, however, must be paid to adjustment of the angle β.

2.1.2 The Image Processor

The system used is a PC-based digital image processor system. The host computer is a *Zenith ZBF-2526* with an *80287* coprocessor running at *12 Mhz*. For digital image processing, frame grabber and frame processor cards are installed in the host computer. The grabber is a Data Translation *DT-2851*. It accepts a single analog input that is either an *NTSC* signal or a *RS-170* signal (*RS-170* is the black and white version of the *NTSC* signal). The resolution of the frame grabber is 480 lines by 512 pixels, and the light intensity resolution is 256 levels. The board has two accessible frame buffers, each can store a full image. External and programmable frame acquisition are possible.

In addition to the above mentioned hardware, a Microsoft FORTRAN Compiler, version 4, was used to manipulate the developed FORTRAN source codes.

2.1.3 The Camera

Two types of systems are used to record moiré fringes. One is a video camera which acquires the pattern and sends it in a standard analog video signal to the image processor for analysis, and the other is a photographic camera which is used to take photographs of the fringe patterns.

The video camera, manufactured by *SONY* (model number *XC-57*), is a *CCD* video module that accepts interchangeable lenses. The camera has a *CCD* image sensor of *510* by *492* pixels. The minimum light sensitivity of the camera is *3* lux at F1.4, which is adequate for the laser power used in the system. Several interchangeable lenses of focal lengths ranging from *1000 mm* to *50 mm*, are also available for viewing field sizes ranging from *50* by *50 mm* down to *2* by *2 mm*.

An *Olympus OM-2S* simple lens reflex camera is used. It has all the

basic photographic functions. Also, a set of objective lenses is available to cover the same field sizes as with the video camera.

Other auxiliaries include a video recorder to record any experiments performed, and a dark room facility to produce photographs of moiré patterns.

2.2 Experiment

2.2.1 Specimens And Experimental Setup

The procedure for preparation of specimens from *CYPRESS* devices includes slicing the device along selected plane in order to expose the chip and the lead frame, Figure 2.1. Two chip sizes, coated and uncoated, are considered. The coefficients of thermal expansion of the chip, leadframe, and encapsulant of the device are shown in Table 2.1. Crossed gratings with a frequency of *1200 lines/mm* in both horizontal and vertical directions are replicated on the specimen surfaces. Uniform heating in all directions is achieved by placing the room temperature specimen into a special oven, Figure 2.2. This equipment possesses precise temperature control and provides a constant temperature.

Table 2.1 The coefficients of thermal expansions of the chip, leadframe, and encapsulant.

Material	Coef. of Thermal Expansion α X 10^6 / C°
Silicon Chip	2.5
Lead Frame	16.3
Encapsulant	19.0

Figure 1.5 displays a schematic view of the experimental equipment. The laser beam is decollimated through a convex lens, purged of *off-axis* reflections by a spatial filter and then collimated to a large beam diameter by means of a parabolic mirror. The resulting expanded beam is then projected onto the specimen at the proper angle β. The second beam, required to create the virtual grating, is generated by reflection of part of the expanded beam by a plane mirror back to the specimen at an angle $-\beta$. For simplicity, Figure 1.5 shows only the optical arrangement used for the monitoring of one displacement component. The other component is obtained by using a second identical arrangement, adjusted for the other field. The second component is superimposed upon the basic one while the specimen

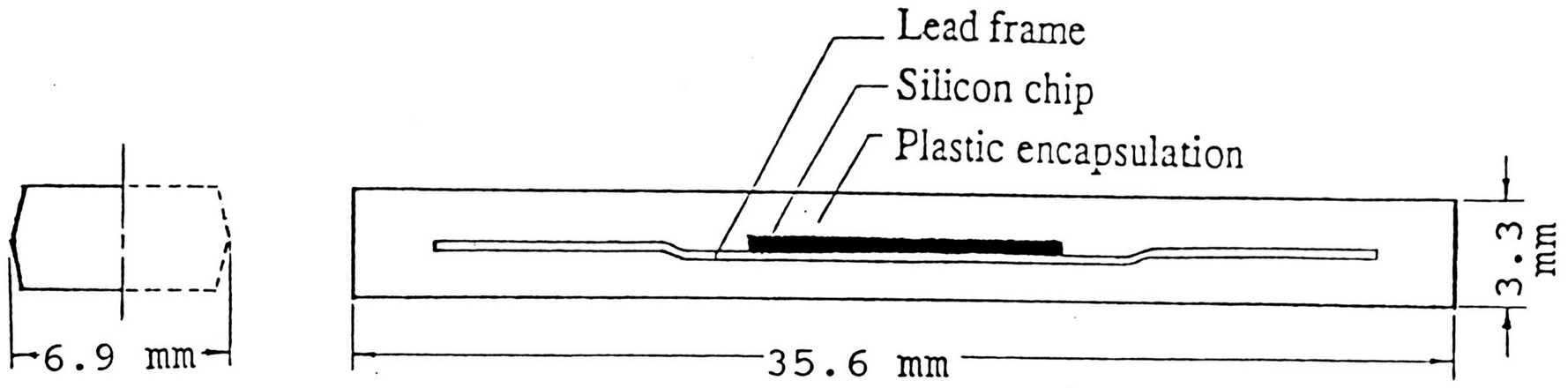

Figure 2.1 Schematic of *CYPRESS* device.

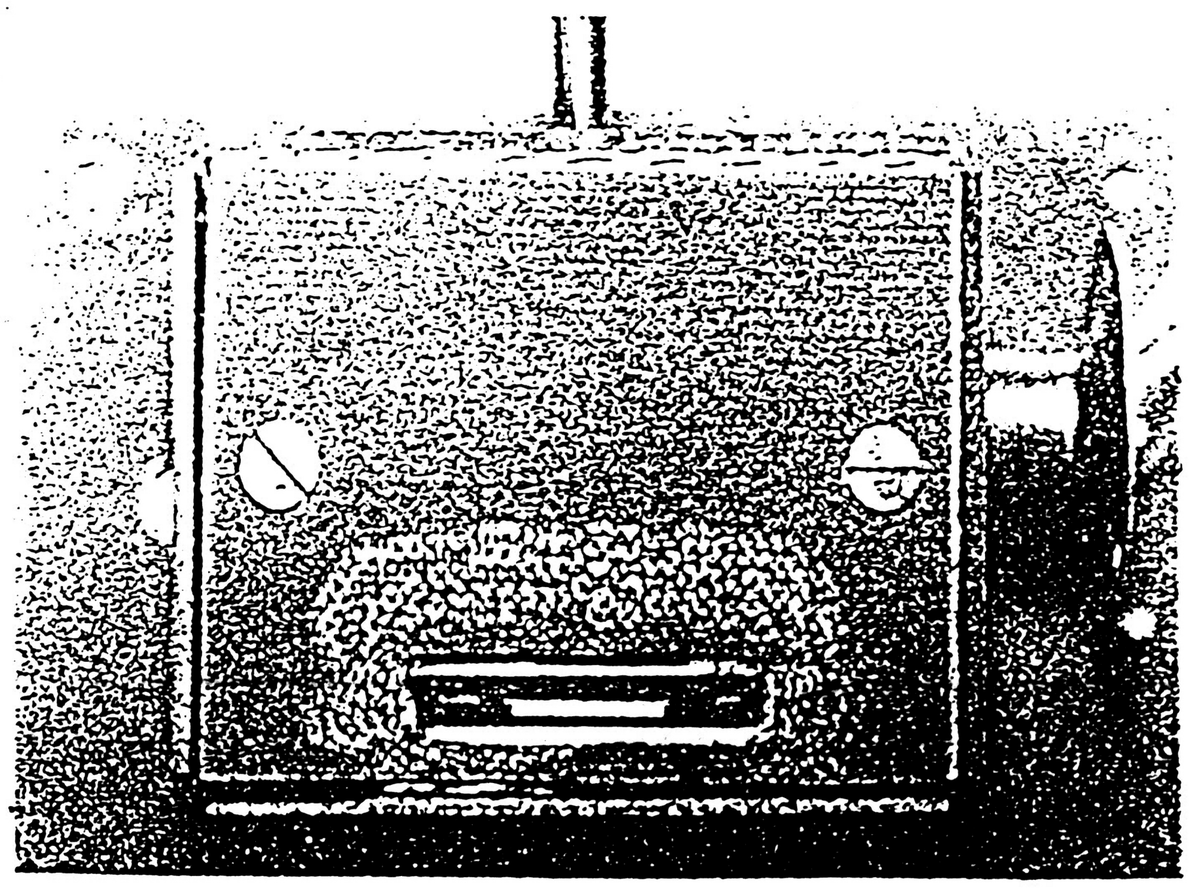

Figure 2.2 Heating device for electronic packages.

remains stationary. Figure 2.3 shows the schematic view of such an arrangement with the specimen illuminated from four directions. Simple optical separation of the two fields becomes necessary for this case. The interference pattern emerging from the specimen is accumulated by a video camera that is connected to a PC-based digital image processor.

2.2.2 Experimental Procedure

The room temperature specimen is placed in the oven. In order to secure a virtual grating frequency of *2400 lines/mm,* the apparatus and specimen are adjusted for proper optical alignment and orientation. In this respect several optical parameters are checked to ensure that the laser beams are projected along the correct angles. In order to eliminate fringe patterns in the camera's view, the lines of the specimen's grating must be parallel to those of the virtual grating for the displacement component of interest. In addition, the camera's optical axis is adjusted to coincide with that of the light wave fronts emerging from the specimen. Actually, some deviations from ideal settings exist in practice. This would result in an initial pattern of relatively few fringes (null or zero field). In that case, the effect of the initial field has to be subtracted from the final displacement field to obtain

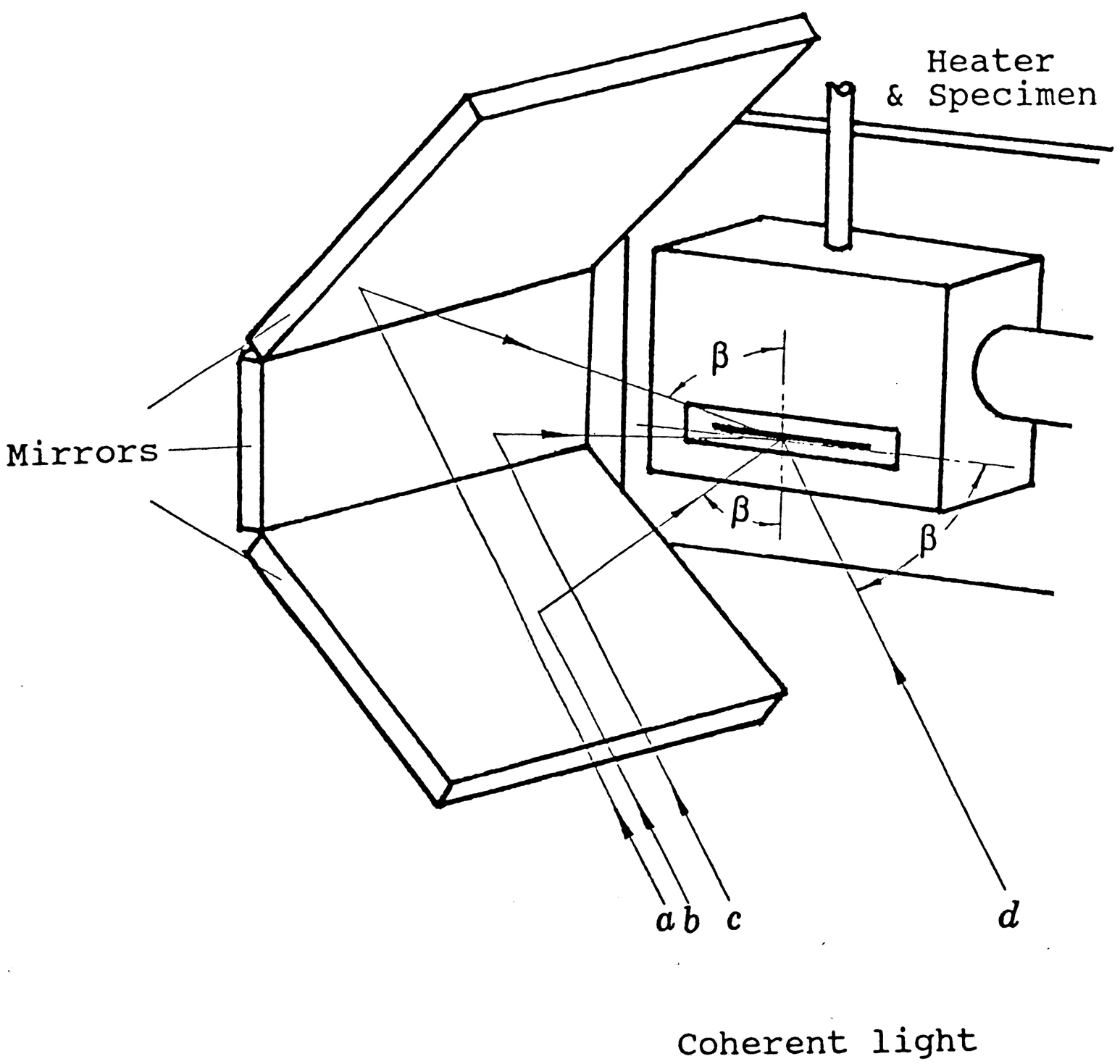

Figure 2.3 Optical arrangement for U and V measurements. Beams a & b produce V-field while beam c & d produce U-field.

the net load induced displacements.

After its null field for each displacement component has been recorded, the specimen is heated in 30 minutes up to $90° C$, while fringe patterns for both displacement components are continuously recorded. The temperature is obtained by placing a thermocouple against one of the lateral sides of specimen, because the fragile grating on specimen surface preventing from placing any measurement instrument on the surface. It has been checked to be within $\pm 1° C$ of the specimen surface temperature.

After the specimen has cooled to room temperature, the initially recorded null field is compared with the resulting null field. This is to verify that the system has kept the proper alignment during the heating operation and that the epoxy has not failed. Then, selected frames representing the evaluation of the deformation are analyzed by means of a fast and accurate image processing software designed to give thermally induced displacements at selected areas from the distribution of the light intensity. This software is also designed to automatically account for the null field.

From the displacement data, the total strains are computed by differentiation of the distributions with respect to the two basic directions,

horizontal *(x)* and vertical *(y)*, using equation (1.3) or (1.4). These equations give the total normal strain components. The net mechanical strains, are due to the inequality in thermal expansion coefficients of the different materials in the package, and are obtained after substraction of the free expansion strain for each material ($\alpha.\Delta T$). Thus:

$$\varepsilon_{x,m} = \varepsilon_x - \alpha.\Delta T$$
$$\varepsilon_{y,m} = \varepsilon_y - \alpha.\Delta T$$
$$\varepsilon_1 = \frac{\varepsilon_{x,m}+\varepsilon_{y,m}}{2} + \sqrt{\left(\frac{\varepsilon_{x,m}-\varepsilon_{y,m}}{2}\right)^2+\left(\frac{\gamma_{xy}}{2}\right)^2} \qquad (2.1)$$
$$\varepsilon_2 = \frac{\varepsilon_{x,m}+\varepsilon_{y,m}}{2} - \sqrt{\left(\frac{\varepsilon_{x,m}-\varepsilon_{y,m}}{2}\right)^2+\left(\frac{\gamma_{xy}}{2}\right)^2}$$

where the subscript in equation (2.1) denotes mechanical strain only and ε_1 and ε_2 are the principal strains.

Chapter 3 : Results And Conclusions

3.1 Results

The fringe patterns of three specimens at *90° C* are shown in Figure 3.1, Figure 3.2 and Figure 3.3, for the left half of the package. For this particular specimen the room temperature was *25° C* and the null field had no fringes for the horizontal direction. Thus, the pattern for the horizontal component shown in Figure 3.1a, Figure 3.2a, and Figure 3.3a is the final contour map of axial displacements *(U)* due to heating. On the other hand, the null field for the vertical direction shown in Figure 3.1b, Figure 3.2b, and Figure 3.3b had several fringes. These must be taken into consideration when processing the final fringe pattern for the vertical displacement component at *90° C* as shown in Figure 3.1c, Figure 3.2c and Figure 3.3c.

Each fringe (dark line) is a line of constant displacement, i.e. all points along that line have undergone the same amount of displacement in the direction considered. To assign fringe values, a reference point of zero displacement must be known. Generally this could be any fixed point of the structure or a boundary point of known displacement. In our case the device

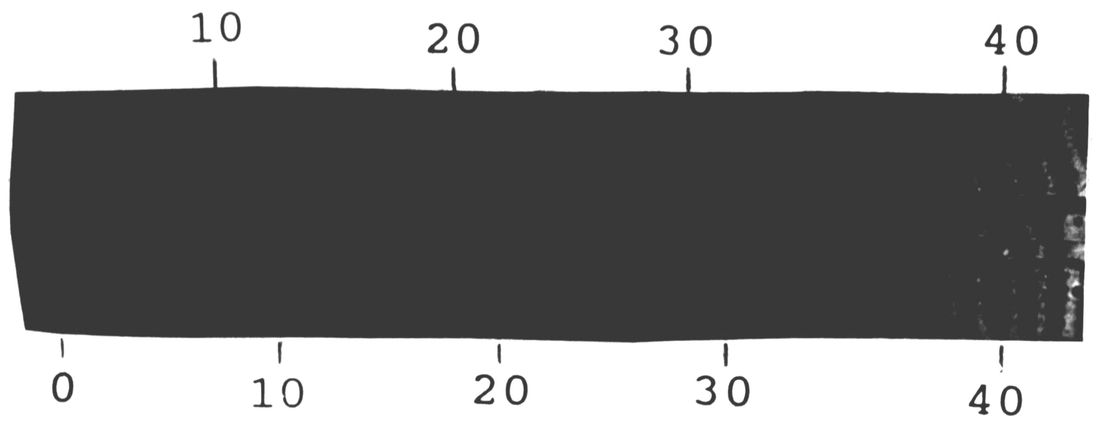

(a)

(b)

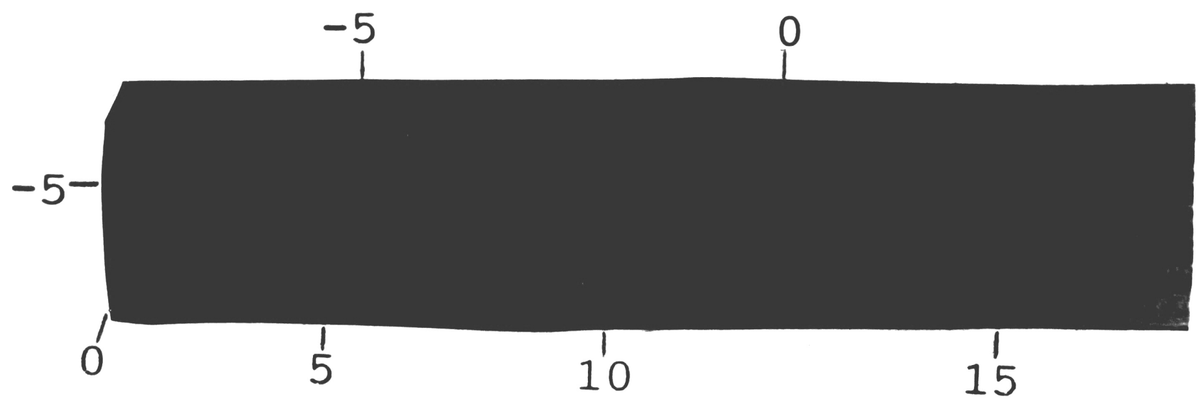

(c)

Figure 3.1 Typical fringe patterns in a long chip non-coated specimen
(a) U-Fringe pattern at 90° C
(b) V-Fringe pattern at 25° C (NULL Field)
(c) V-Fringe pattern at 90° C

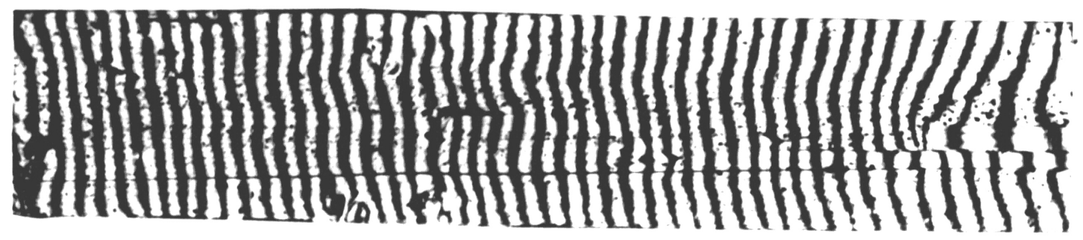

(a)

(b)

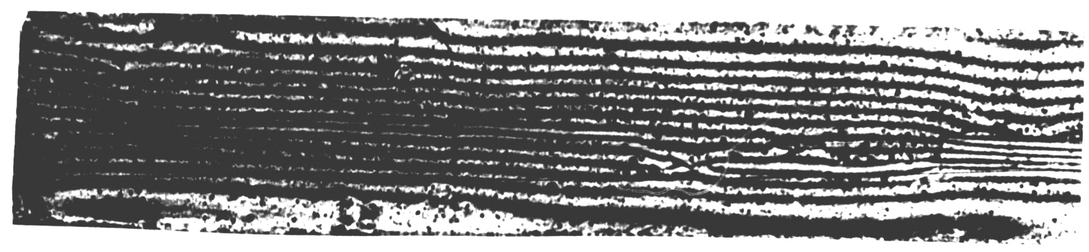

(c)

Figure 3.2 Typical fringe patterns in a short chip non-coated specimen
(a) U-Fringe pattern at 90° C
(b) V-Fringe pattern at 25° C (NULL Field)
(c) V-Fringe pattern at 90° C

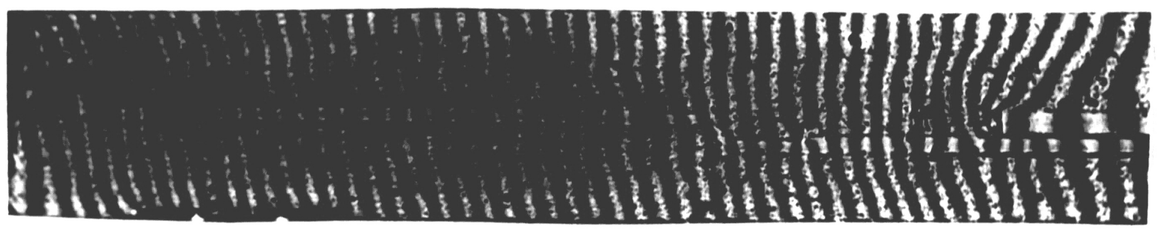

(a)

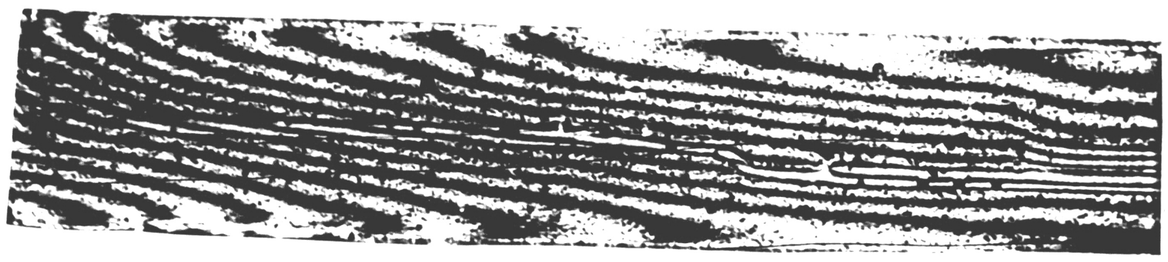

(b)

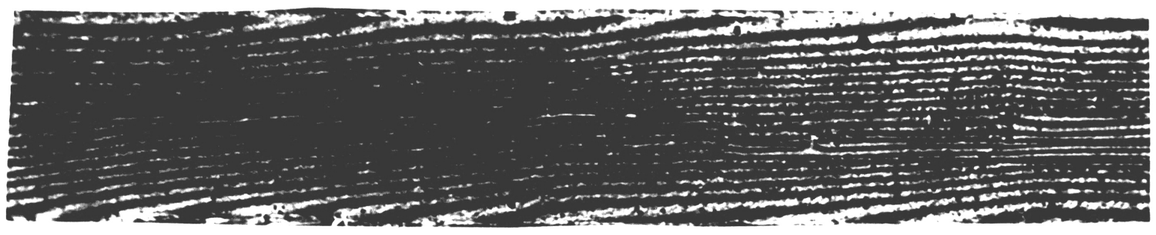

(c)

Figure 3.3 Typical fringe patterns in a short chip coated specimen
(a) U-Fringe pattern at 90° C
(b) V-Fringe pattern at 25° C (NULL Field)
(c) V-Fringe pattern at 90° C

was not constrained at any point and was free to expand in all directions. Therefore, any arbitrary point may be considered as a reference point and all displacements may be measured relative to it. For analysis of strains, the reference point displacement is immaterial, since only relative displacements are needed for the strain computations (equation (1.4)) and not the absolute values. The lower left corner of the package was considered the reference point in this example. Fringes passing through it were assigned the order zero and all other fringe orders were counted relative to that point with orders increasing in the positive directions of the reference axes. The assigned fringe orders are also shown in Figure 3.1a, 3.1b, and 3.1c.

As there is clear evidence that there are strain concentrations at the chip edges, as seen in Figure 3.1, Figure 3.2 and Figure 3.3; studying this region is most suitable for determining the effect of the package parameters on thermal strain in an electronic package. Numerical values for displacements at the chip edge, Figure 3.4, are found by using fractional fringe analysis, then are smoothed by forth order least square fitting, and are stored in displacement data files. In Figure 3.5 and Figure 3.6, horizontal displacements *(U)* and vertical displacement *(V)* along the line *(a - b)* as measured from *a* to *b* are plotted for three different specimens. Similarly, in Figure 3.7 and Figure 3.8, two components of displacement *(U* and *V)* across

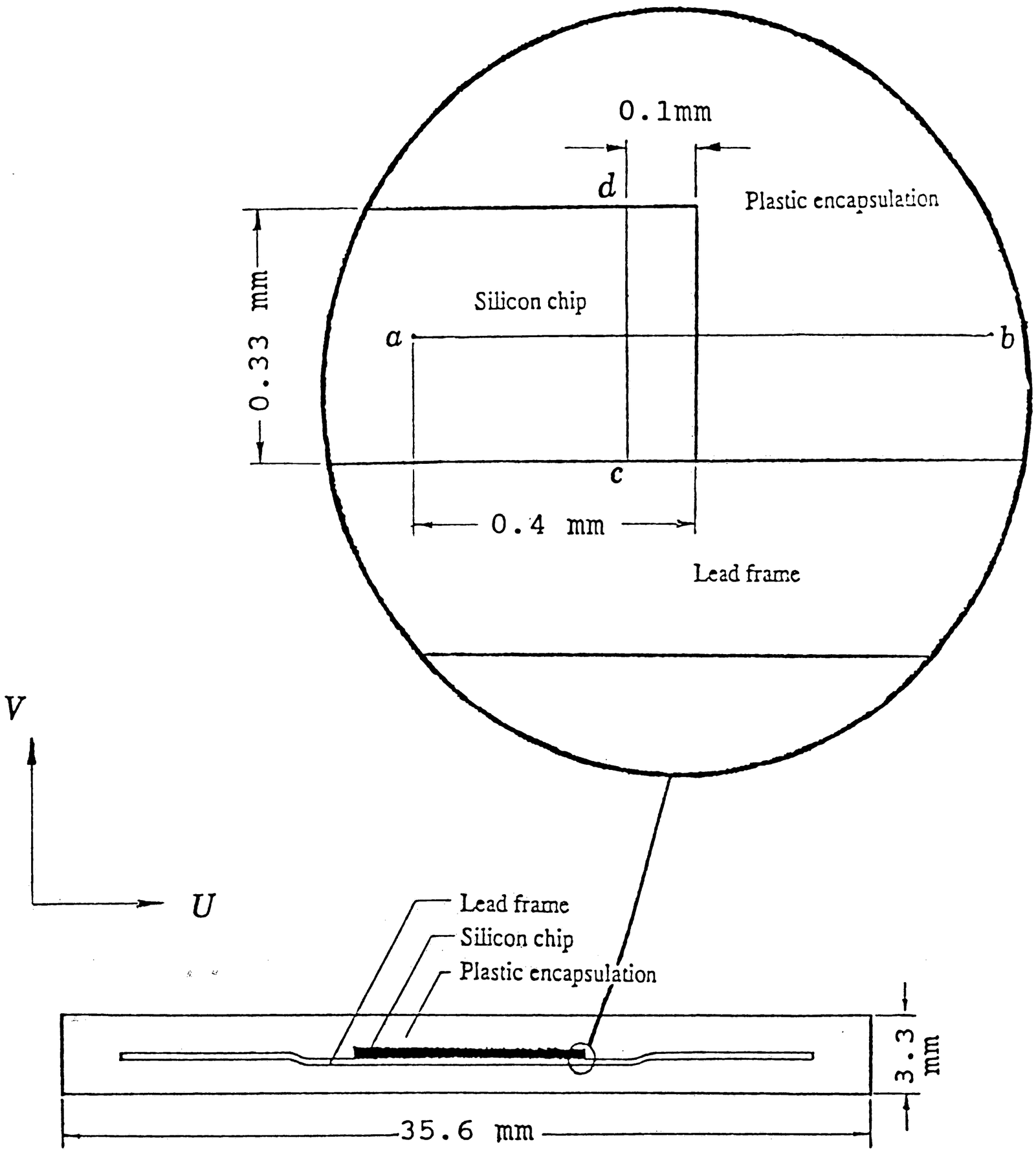

Figure 3.4 Schematic of *CYPRESS* device

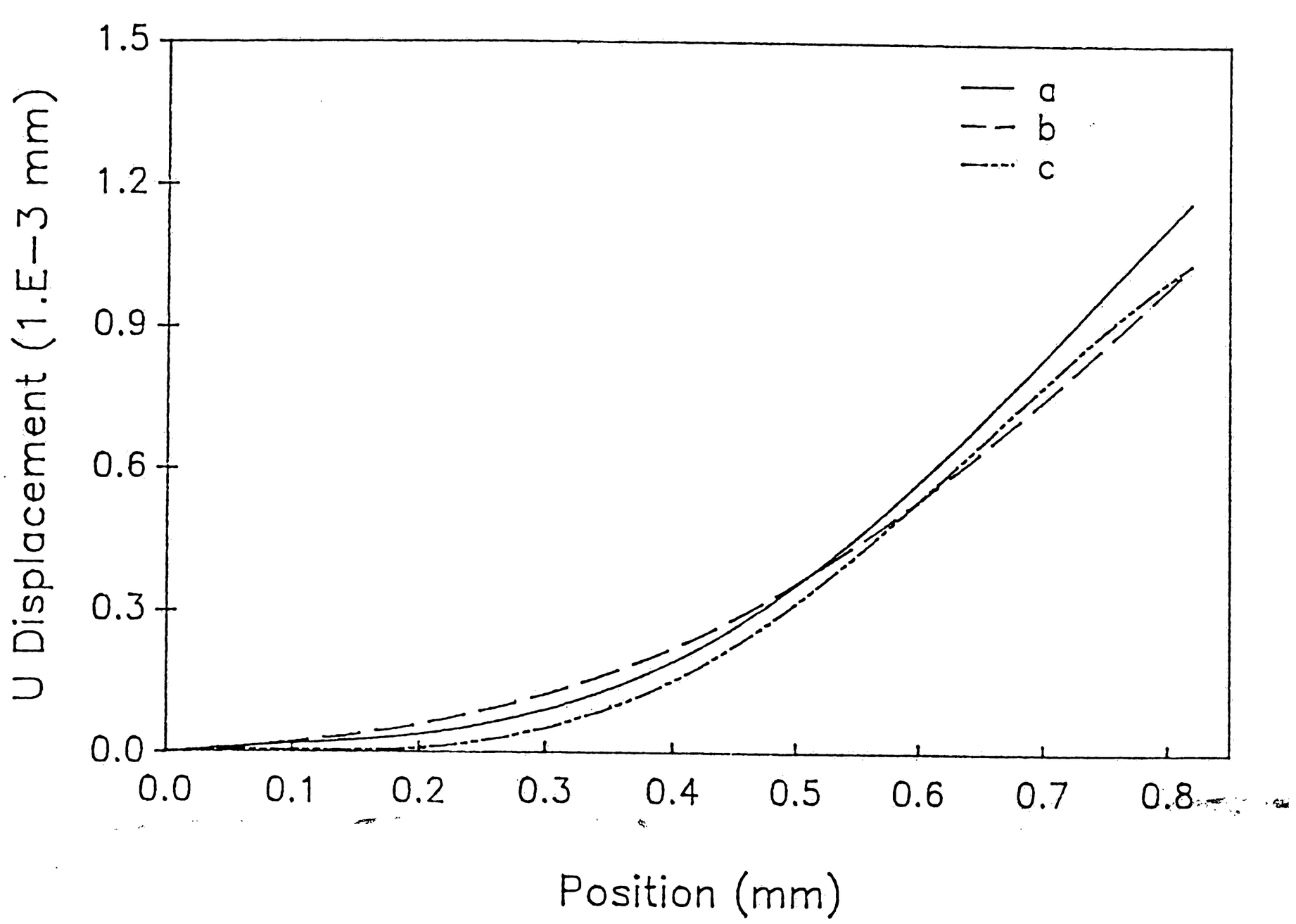

Figure 3.5 Net displacement distributions along line *a* - *b*. (a) long chip non-coated specimen. (b) short chip non-coated specimen. (c) short chip coated specimen.

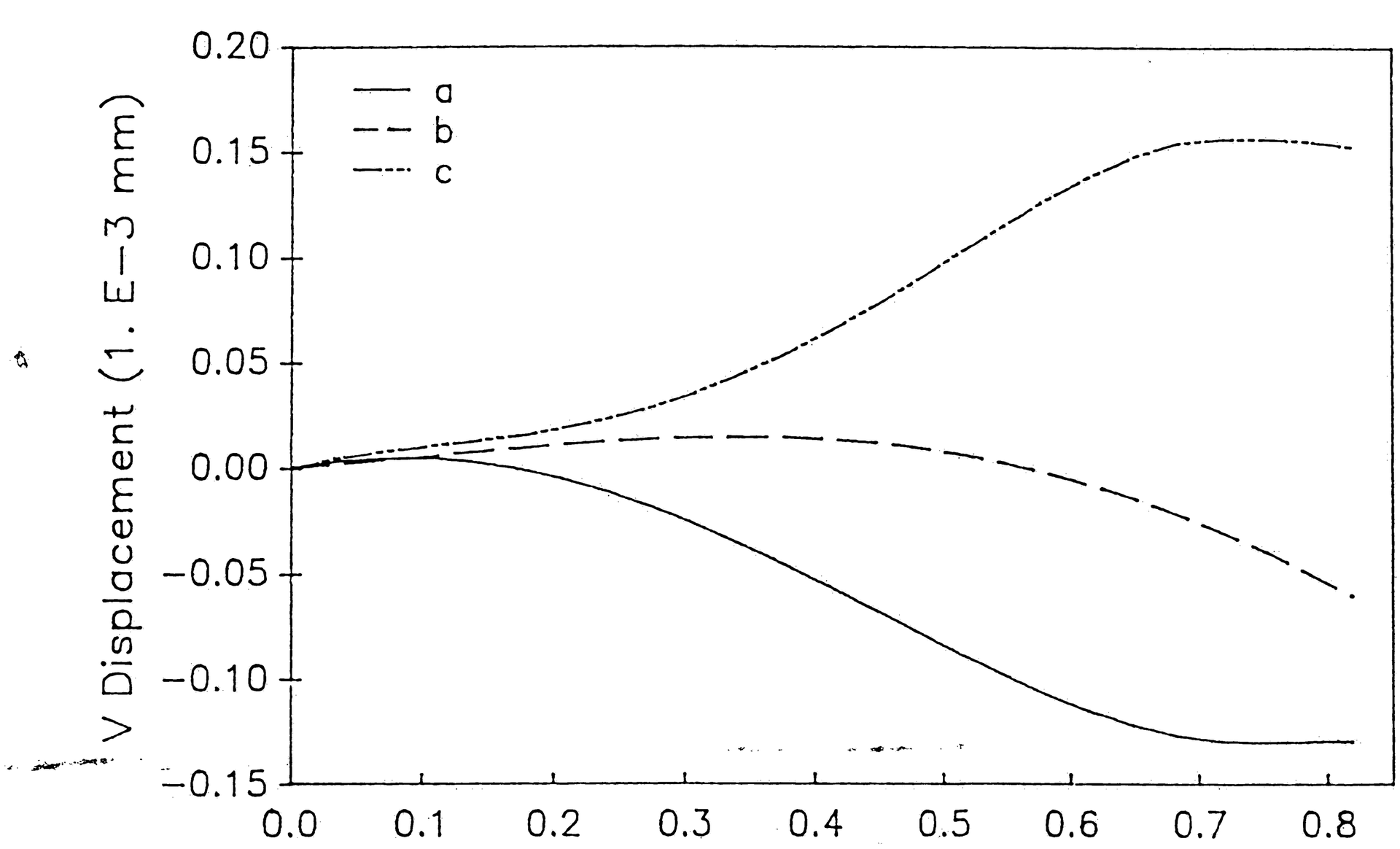

Figure 3.6 Net displacement distributions along line *a* - *b*. (a) long chip non-coated specimen. (b) short chip non-coated specimen. (c) short chip coated specimen.

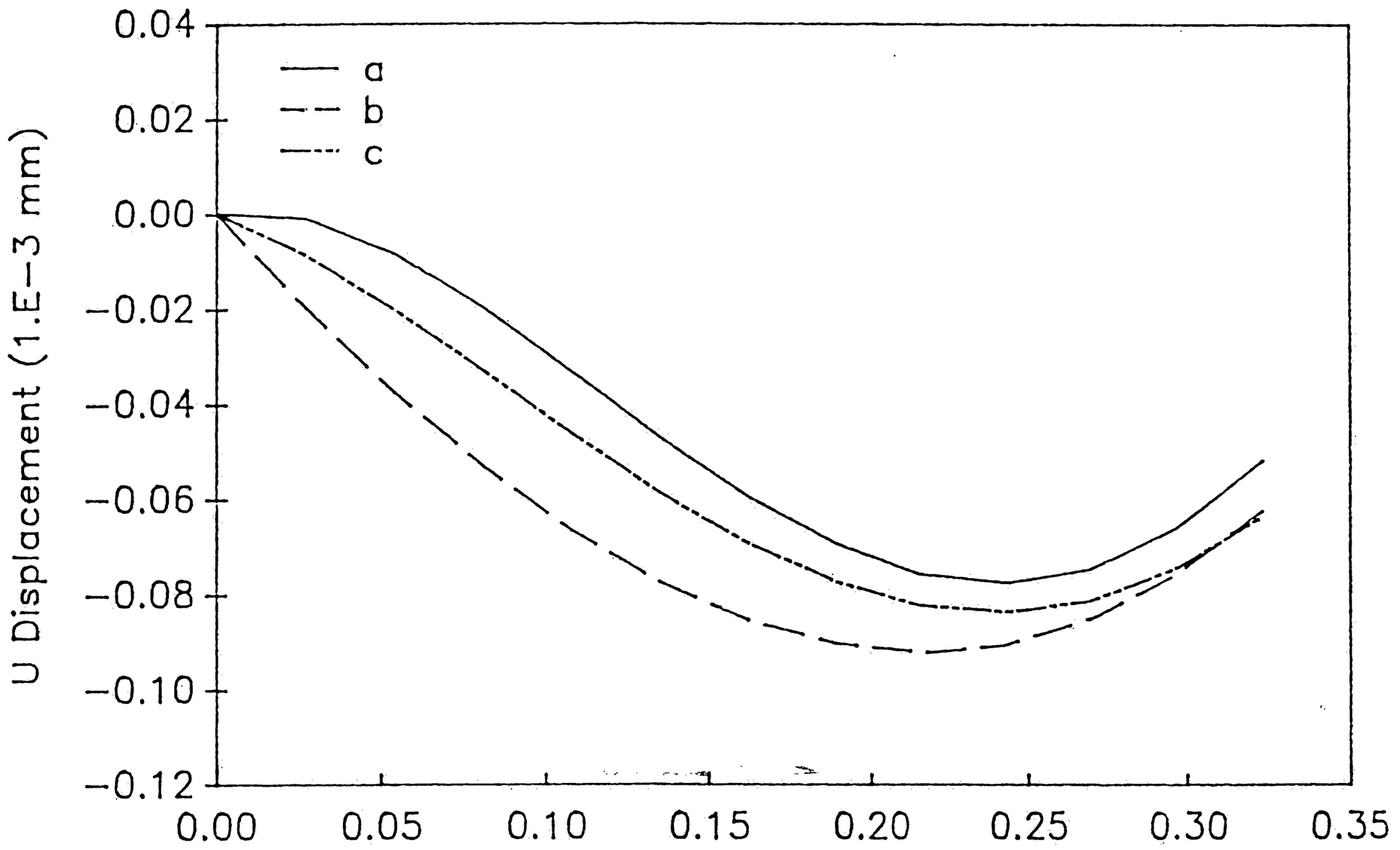

Figure 3.7 Net displacement distributions along line *c* - *d*. (a) long chip non-coated specimen. (b) short chip non-coated specimen. (c) short chip coated specimen.

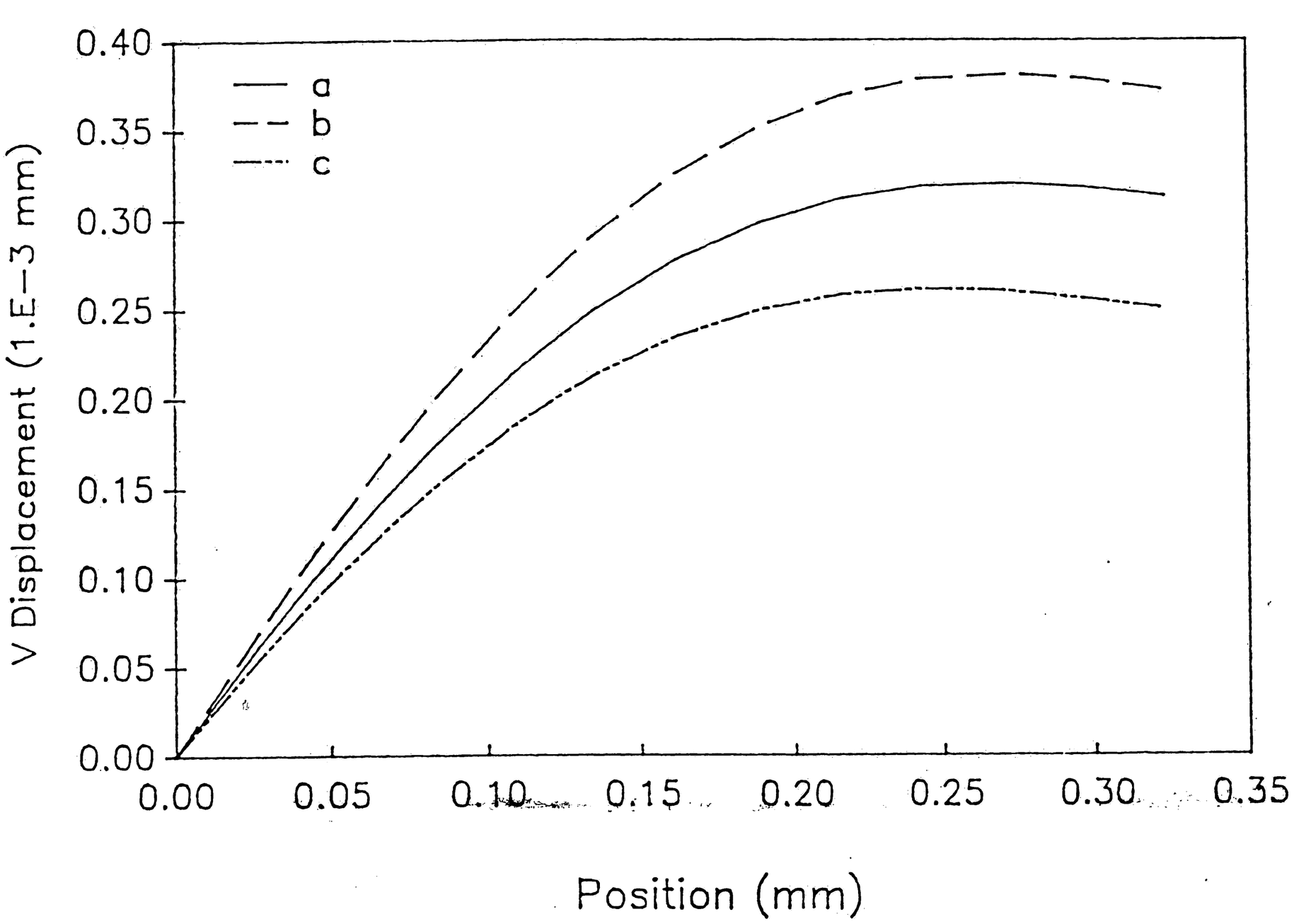

Figure 3.8 Net displacement distributions along line *c* - *d*. (a) long chip non-coated specimen. (b) short chip non-coated specimen. (c) short chip coated specimen.

the chip thickness along the line *(c - d)* as measured from *c* to *d* are plotted, assuming zero displacement at points *a* and *c*, correspondingly.

By comparing the displacement data, it is found that the normal strains are much higher than the shear strains. This implies that the package will fail under the normal strains which are caused by bending moment due to the mismatch in the coefficients of thermal expansion in the package.

The principal strains are calculated from equation (2.1) and the results for the principal strains along *a - b* and *c - d* are plotted. We consider a first specimen with leadframe and chip inside and a second with only leadframe inside. By comparing the strains in these two different specimens, the curves in Figure 3.9 and Figure 3.10 respectively show that the mechanical strains which are due to mismatch in the coefficients of thermal expansions of the chip, leadframe, and encapsulant are on the order of thousands microstrains. This implies that the there is a severe strain concentration in a package under thermal loads.

Figure 3.11 ,Figure 3.12, Figure 3.13 and Figure 3.14, reflect the effect of chip size and coating on the strain levels. Clearly the strain concentration

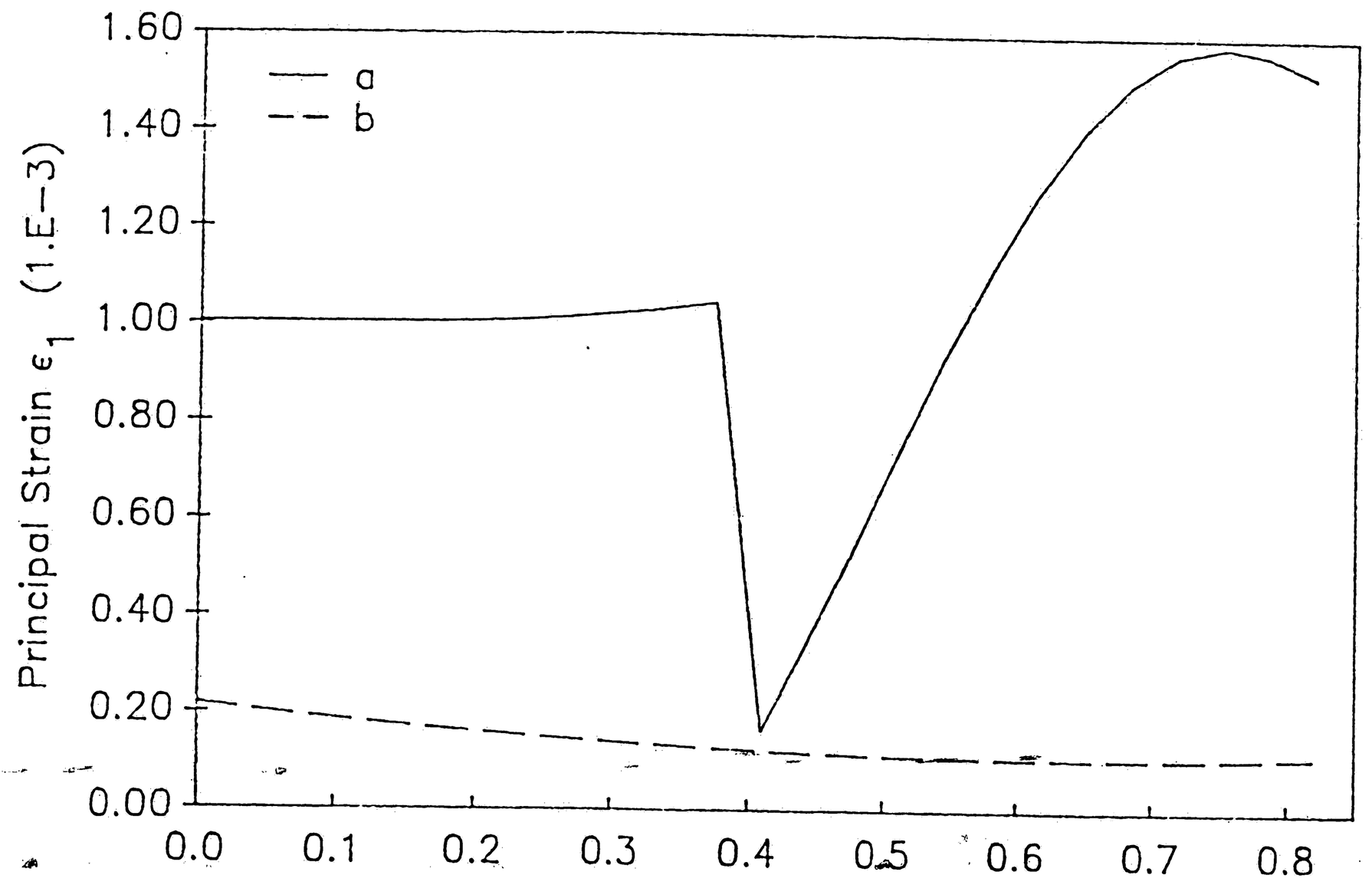

Figure 3.9 Principal strain distributions along line *a* - *b*. (a) Full package (i.e. include chip and leadframe). (b) leadframe only.

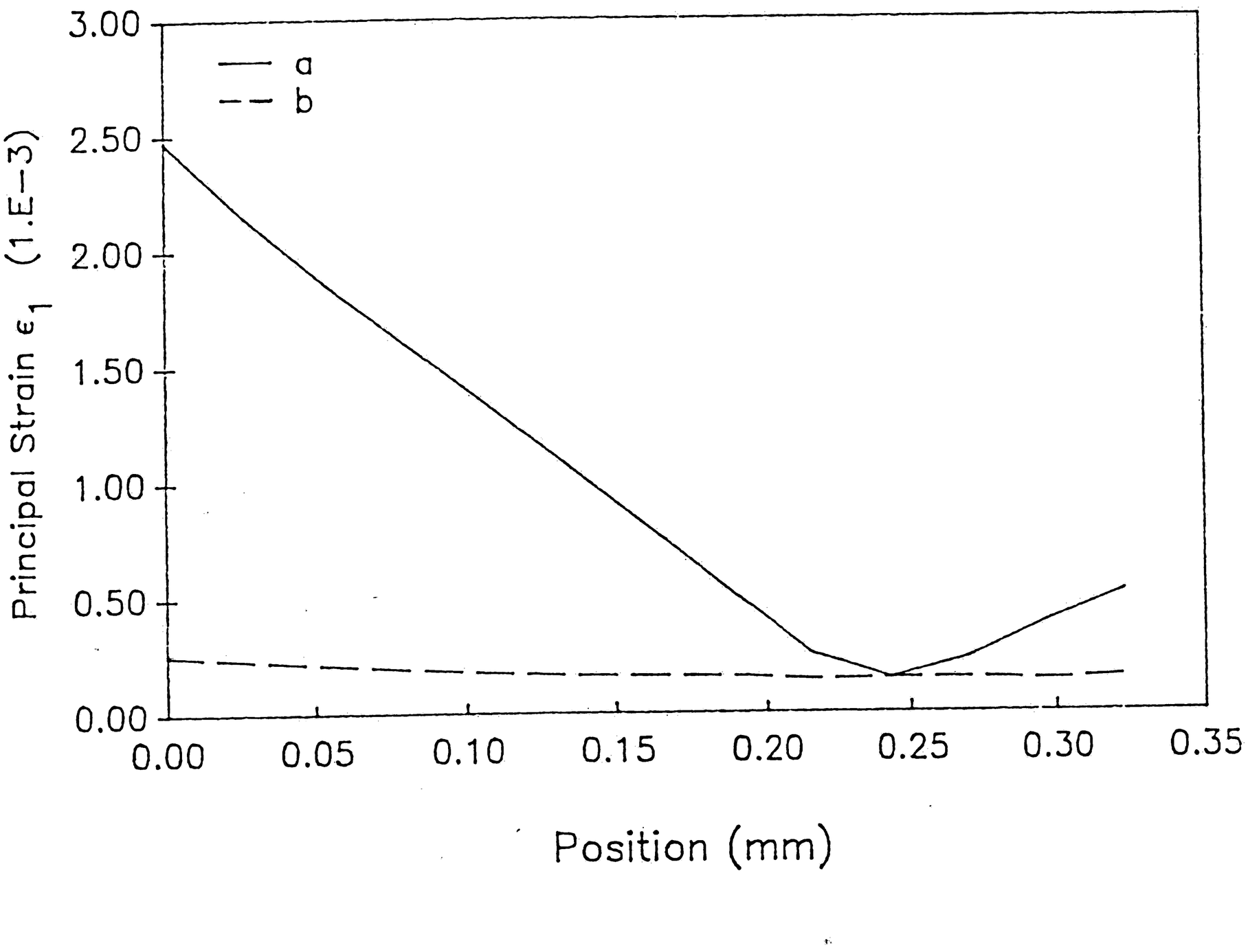

Figure 3.10 Principal strain distributions along line *c* - *d*. (a) Full package (i.e. include chip and leadframe). (b) leadframe only.

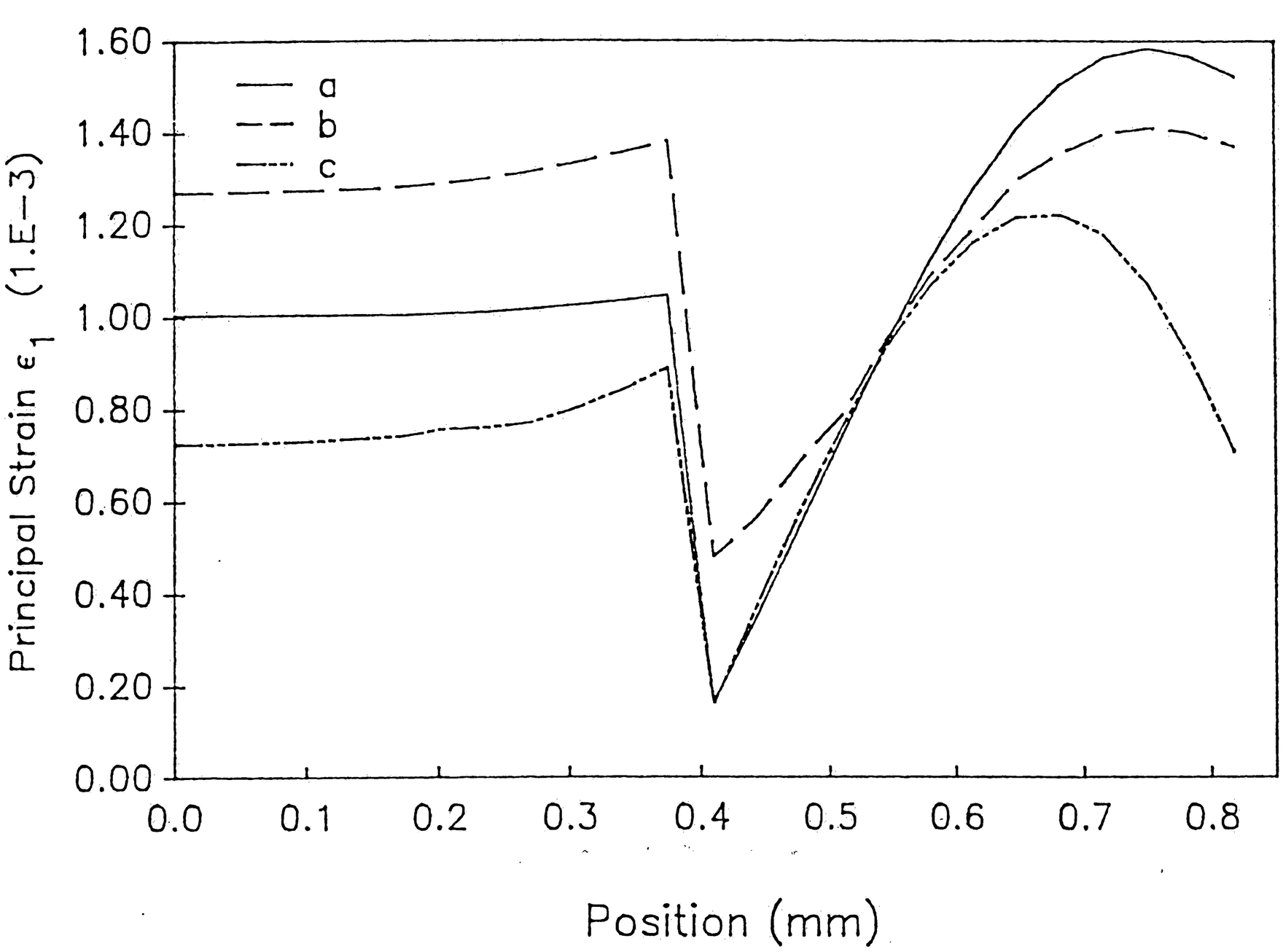

Figure 3.11 Principal strain distributions along line *a* - *b*. (a) long chip non-coated specimen. (b) short chip non-coated specimen. (c) short chip coated specimen.

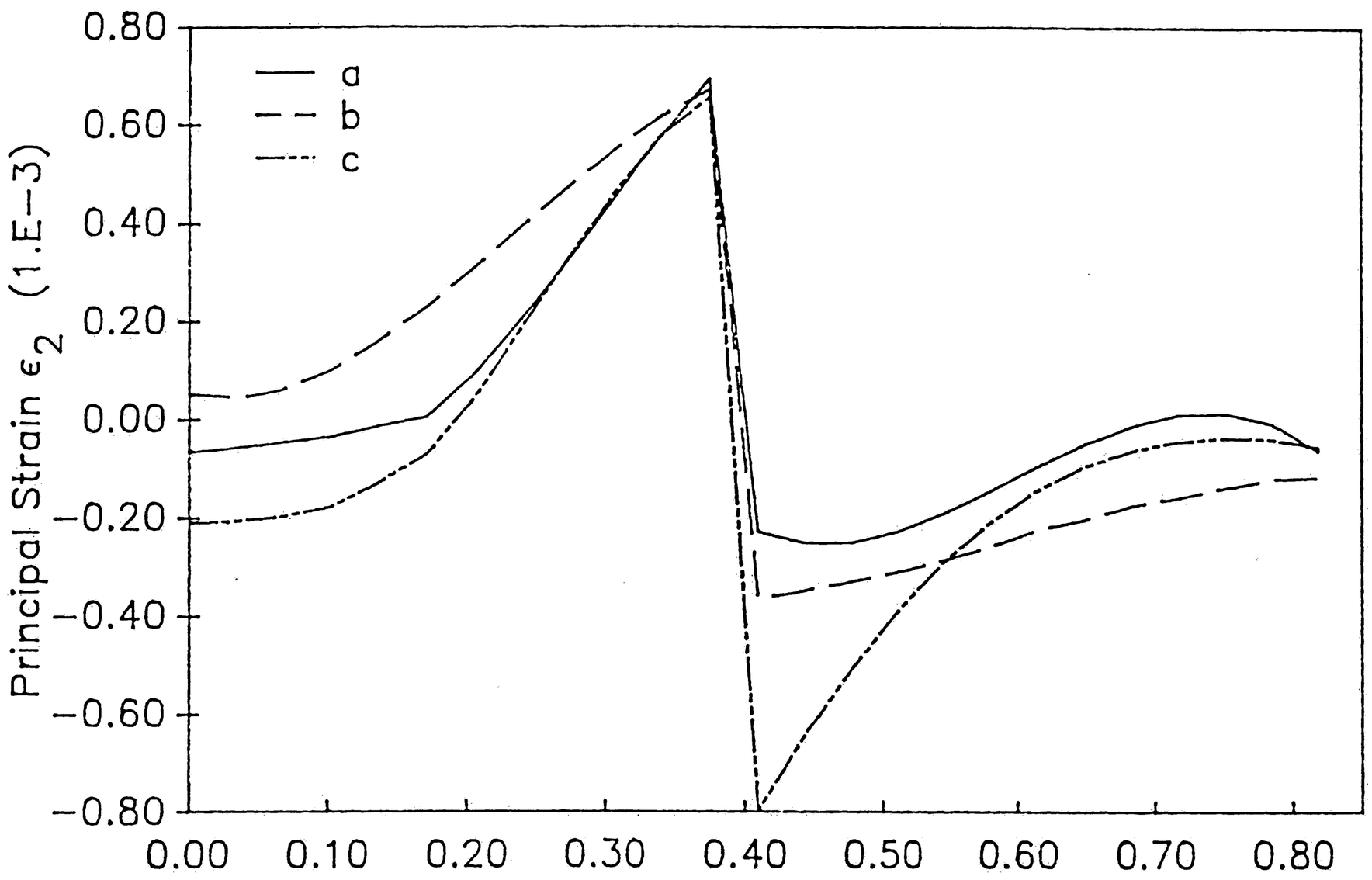

Figure 3.12 Principal strain distributions along line *a* - *b*. (a) long chip non-coated specimen. (b) short chip non-coated specimen. (c) short chip coated specimen.

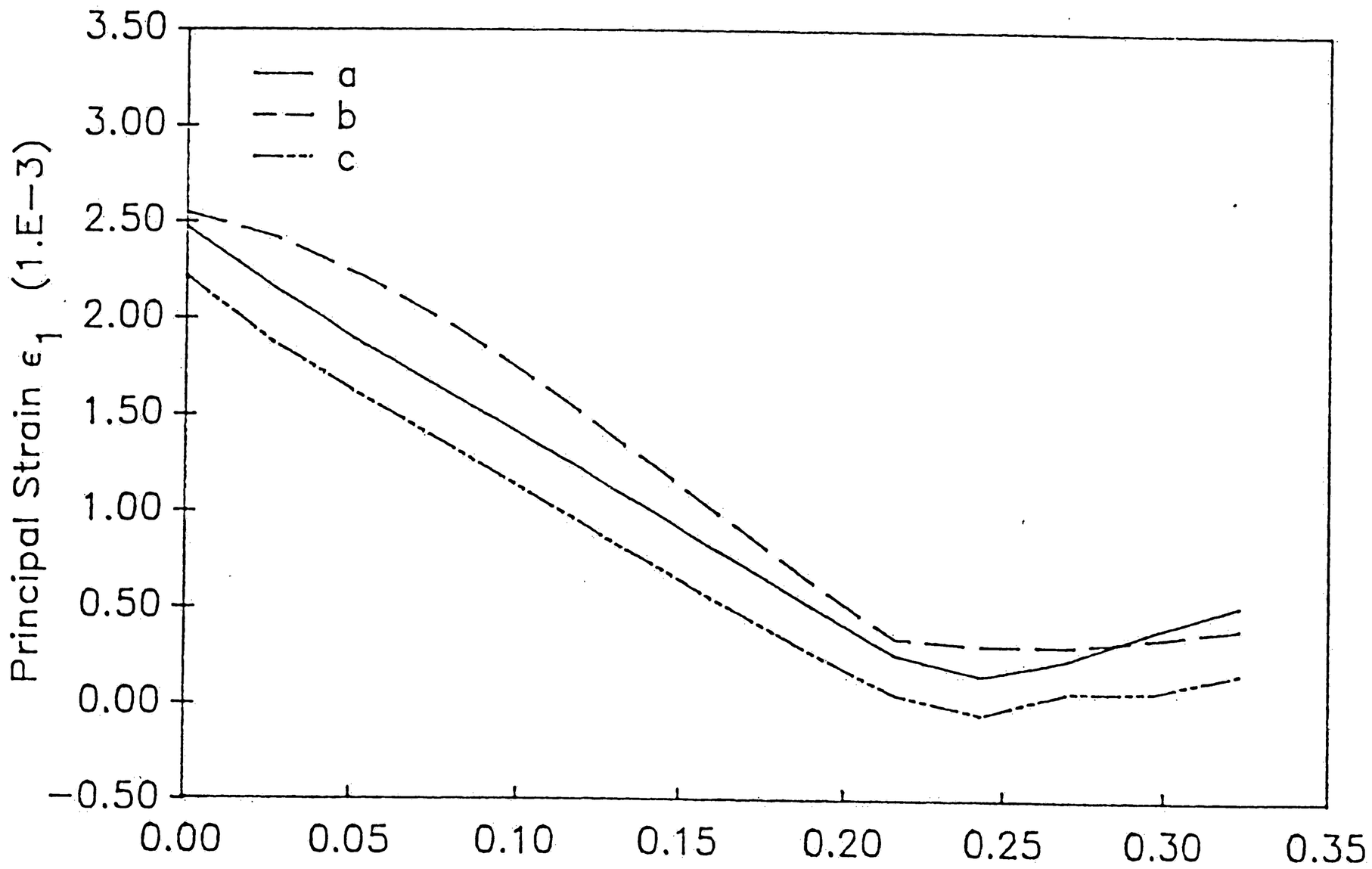

Figure 3.13 Principal strain distributions along line *c* - *d*.(a) long chip non-coated specimen. (b) short chip non-coated specimen. (c) short chip coated specimen.

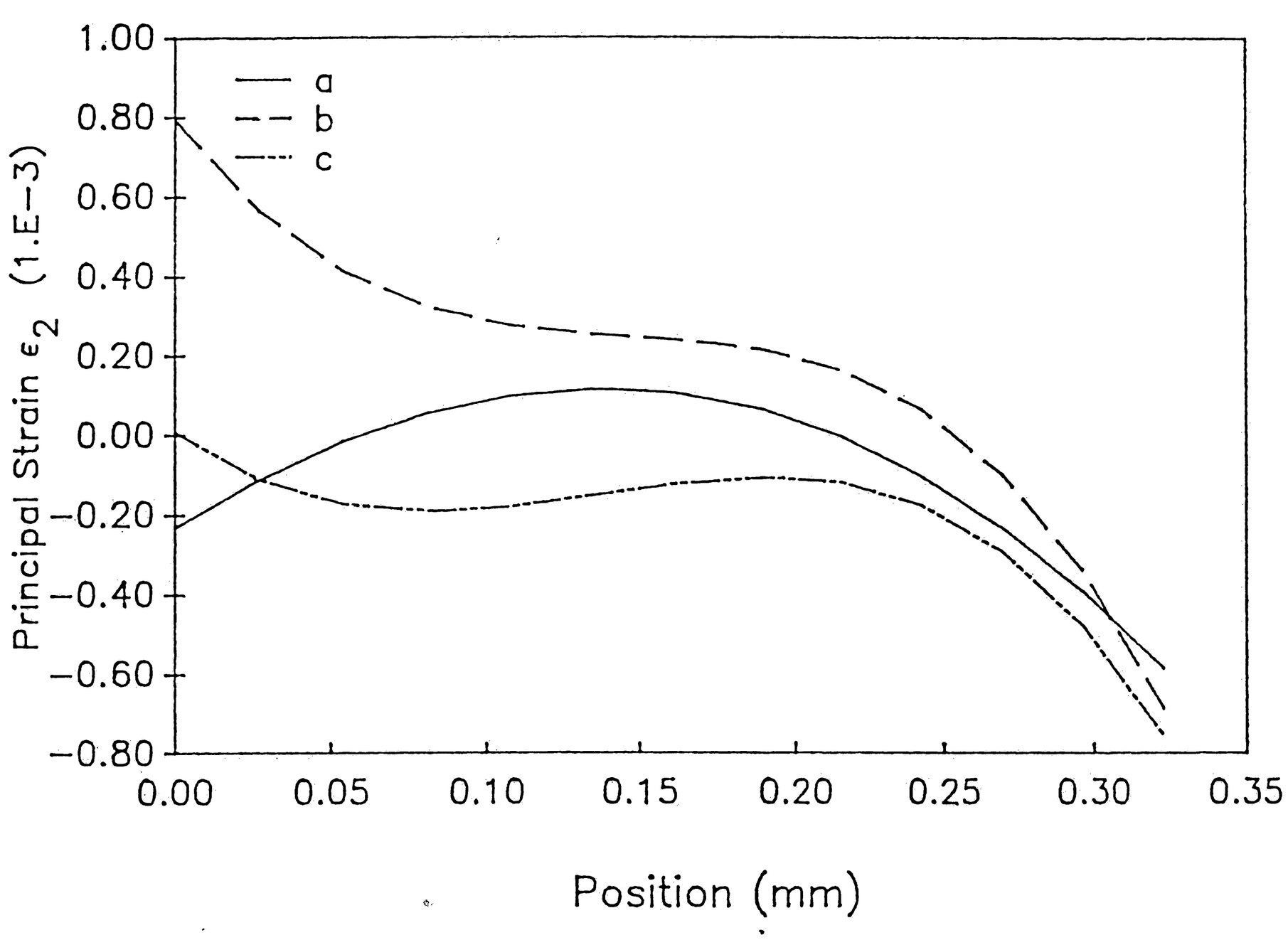

Figure 3.14 Principal strain distributions along line *c* - *d*. (a) long chip non-coated specimen. (b) short chip non-coated specimen. (c) short chip coated specimen.

in the long chip specimen is lower than those in the short chip specimen. If the chip is coated, the specimen strain levels under consideration are reduced almost *35%*. Also Figure 3.11 and Figure 3.12 show that there are all tensional strains applied at the region nearby the edge due to thermal load. The highest strains took place at bottom edge of chip, as seen in Figure 3.13. This high concentrated strains may cause the package's failure at a temperature different from the expected temperature. The compression strain applied on the top of the chip is seen in Figure 3.14. These results could be important for package design.

In fractional fringe analysis, the determination of intermediate displacements over any half fringe is based on light intensity measurements which may have some degree of uncertainty (error). The uncertainty level for the displacements, depends on the weight and uncertainty of each measured parameter involved. It could be concluded that the uncertainty level is below *±0.5%* for the displacements determined by fractional fringe analysis [12]. Also, some errors are introduced by curve fitting the displacement data for computing the numerical values for the strain field. A typical example is shown in Figure 3.15 and Figure 3.16.

Figure 3.15 and Figure 3.16 show that the larger errors are introduced

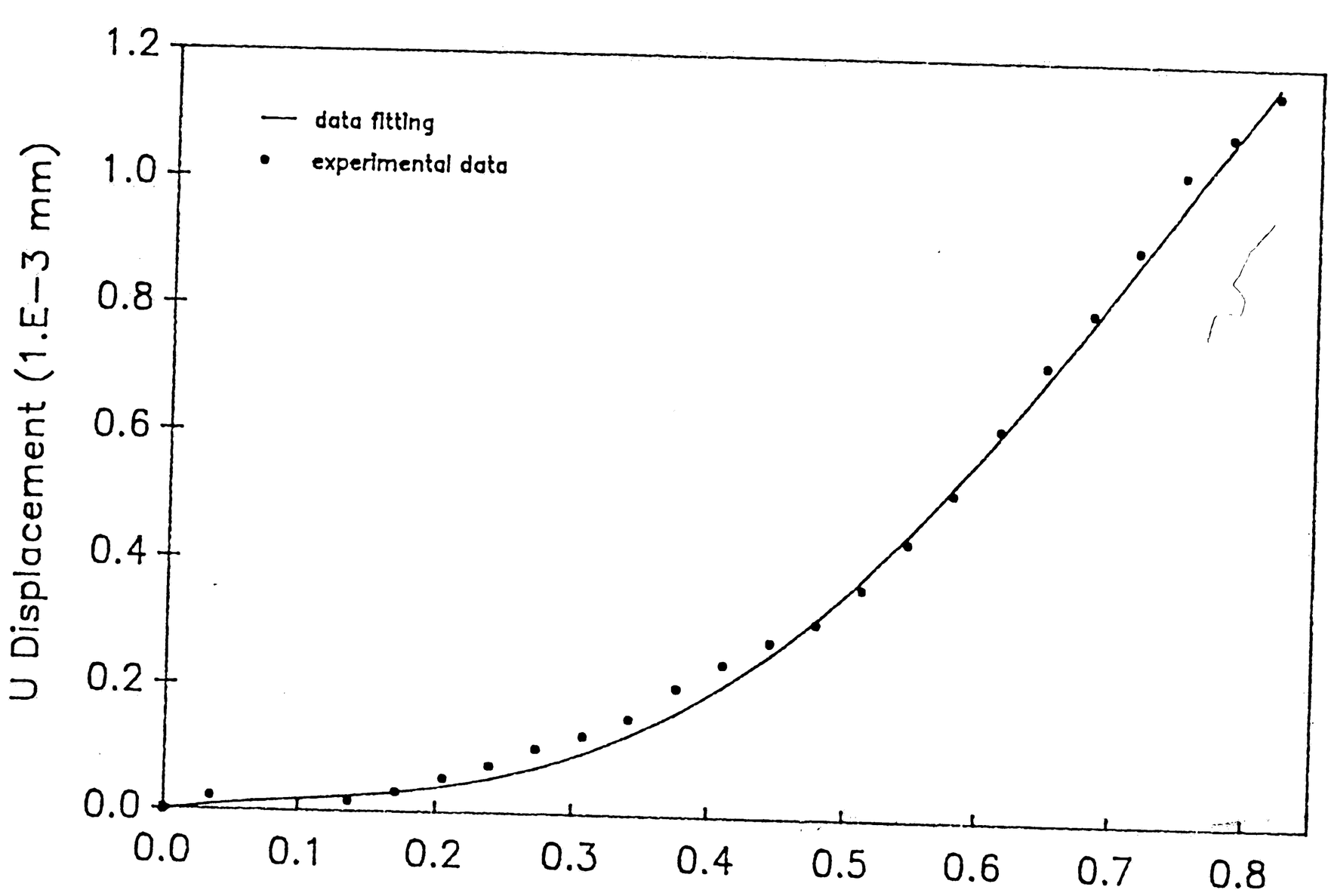

Figure 3.15 A typical error estimation of the displacement distributions along line *a* - *b*.

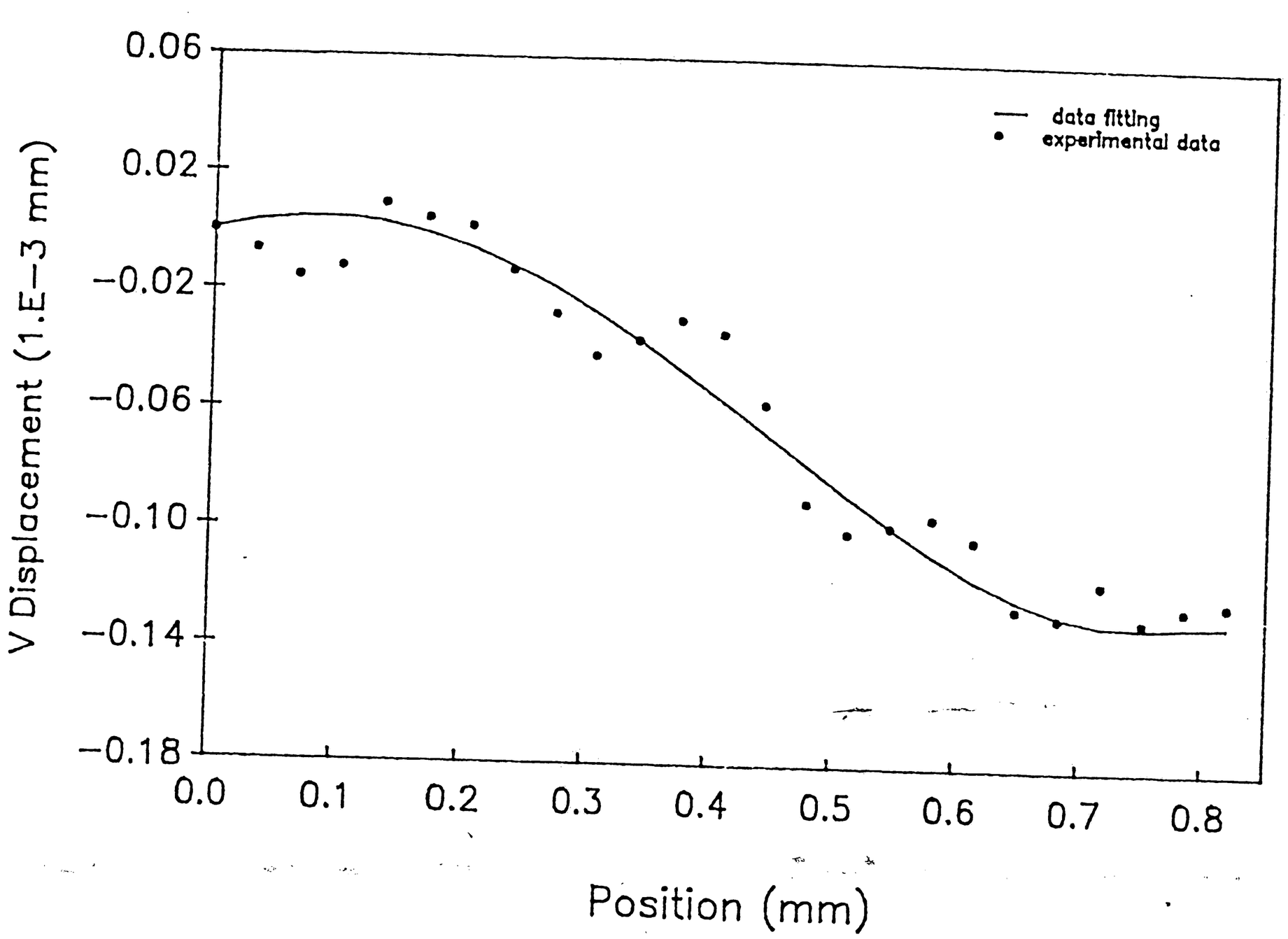

Figure 3.16 A typical error estimation of the displacement distributions along line *a* - *b*.

while the V displacement distributions are estimated along the horizontal direction. This results from the measurements' procedures. To measure horizontal displacements field, we scan the moiré pattern row by row.Thedata of U displacement distributions along the horizontal direction are obtained from one scan and are quite smooth by using the fractional fringe analysis technique. To measure vertical displacement field, we scan the pattern column by column. The data of V displacement distribution along the horizontal direction are unsmooth since the data are obtained by scanning different column. Similarly in the other direction, we will get larger errors while estimating the U displacement distributions along the vertical direction.

In addition to the above mentioned factors of the error, the $\pm 1^{\circ}$ C of temperature difference also introduce some uncertainty in the results. For quantitative analysis, it may be safely concluded that the errors of the final result are between $\pm 5\%$.

3.2 Conclusions

Due to the complexity of the package geometry and the boundary

conditions, many analytical and numerical assessments of packages under thermal loads are not completely successful. Also the small magnitude of the deformations due to the loading conditions in electronic packages make the detection very difficult for many deformation measuring techniques. Moiré interferometry fills the gap in capabilities of other techniques, in as much as it can be used for measurements in both macromechanics and micromechanics domains.

Full displacement fields at chip corners in electronic devices subject to uniform heating were successfully measured by moiré interferometry enhanced by digital image processing. The principal strains were computed from the field data, and their distributions were determined and analyzed. The effect of the chip sizes and coating on strain levels are successfully assessed. The investigations revealed a very interesting result that is the long chip specimen has lower strains than the short one. A possible cause is that the short chip specimen may have larger curvature under the thermal load due to the mismatch in the coefficients of different materials in the package. These experimental data provide an important reference for package design.

Fractional Fringe Moiré Interferometry yields realistic and accurate

full displacement field data. It may therefore be used for various applications in the microelectronics industry, namely, design, testing and evaluation processes. Evidence has also been given for the potential of the method as a basic deformation monitoring tool.

References

1. J.Guild, "The Interference System of Crossed Diffraction Gratings", Clarendon Press, Oxford, England, 1956.

2. D. Post, "optical Interference for Deformation Measurements-Classical, Holographic and Moiré Interferometry", in Mechanics of Nondestructive Testing, ed. by W.W. Stinchcomb, Plenum Press, New York, pp. 1-53, 1980.

3. E.M. Weissman, and D. Post, "Full-Field Displacement Rossette by Moiré Interferometry", Experimental Mechanics, vol.22, no.9 ,pp.324 - 328, 1982.

4. D.Post, "Moiré Interferometry at VPI and SU, "Experimental Mechanics, vol.23, no.2, pp.203 -210, 1983.

5. M.S. Dadkhah, F.X. Wang, and A.S.Kobayashi, "Simultaneous On-Line Measurement of Orthogonal Displacement Fields by Moiré Interferometry",Experimental Techniques,vol.12, no.7, pp. 28 -29, 1988.

6. D. Post, and W.A. Baracat, "High-Sensitivity Moiré Interferometry - A Simplified Approach", Experimental Mechanics, vol. 21, no.3, pp. 100 -104, 1981.

7. M.L.Basehore, and D.Post, "High-Frequency, High-Reflectance Transferable Moiré Gratings",Experimental Techniques. vol. 8, no.5, pp.29-31, 1984.

8. A.McDonach, J.McKelvie, P. MacKenzie, and C.A.Walker, "Improved Moiré Interferometry and Applications in Fracture Mechanics, Residual Stress and Damaged Composites",Experimental Techniques,vol.23, no.2, pp.20 - 24, 1983.

9. D.Post, "Developments in Moiré Interferometry", Optical Engineering, vol.21, no.3, pp.458 -467, 1982.

10. M. Basehore, and D. Post, "Moiré Method for In-Plane and Out-of-Plane Displacement Measurements, Experimental Mechanics, vol. 21, no.9, pp.321 - 328, 1981.

11. A.S.Voloshin, C.P.Burger, R.E.Rowlands, and T.S.Richard,"Fractional Moiré Strain Analysis using Digital Imaging Techniques", Experimental Mechanics, vol.26, no.1, pp.254-258, 1986.

12. A.F. Bastawros, "Enhancement of Moiré Interferometry by Digital Image Processing", Ph.D. dissertation, 1990.

Vita

Pei-Haw Tsao was born in Taiwan, Republic of China on July 23, 1963. He is highly expected as the first son of Ching-Yang and Chang-Chung Tsao.

After graduating from Shin-Chu Public High School, he join the Department of Mechanical Engineering of Tamkang University, where he obtained his B.S. in 1985. During this period, he had be selected, with high honors, as an executive committee of Student Division of Chinese Engineer Society.

Pei-Haw had two year military service after his graduation and served as technical sergeant in department of Research and Development. He then worked as an assistant engineer in Victory Industrial Company. He came to Lehigh University to pursued his Master of Science in mechanical engineering in 1988.